ELSEVIER

Remote Sensing of Environment

http://www.elsevier.com/locate/rse

(This is a sample cover image for this issue. The actual cover is not yet available at this time.)

A sub-pixel-based calculation of fire radiative power from MODIS observations: 2. Sensitivity analysis and potential fire weather application

David Peterson *, Jun Wang

Department of Earth and Atmospheric Sciences, University of Nebraska—Lincoln, Lincoln, NE 68588, USA

ARTICLE INFO

ABSTRACT

Fire radiative power (FRP) over a pixel area has been highlighted as a valuable parameter for quantitatively deriving smoke emissions. However, smoke plume rise forecasts and characterizations of fire intensity require additional information, including the FRP over the fire area (FRP_f) and per fire area (or fire radiative flux), both of which can be calculated through a bi-spectral retrieval of sub-pixel fire area and temperature. This study, the second in a two-part series, examines the sources of error and the corresponding uncertainties in a sub-pixel algorithm that calculates FRP_f for fire pixels identified at 1 km² nominal spatial resolution by the MODerate Resolution Imaging Spectroradiometer (MODIS) fire detection algorithm (collection 5). Radiative transfer simulations are incorporated to account for atmospheric effects as a function of Earth-satellite geometry at 3.96 and 11 μm (MODIS fire detection channels), and show that the 11 μm channel is highly sensitive to variations in column water vapor amount. By investigating several fire events in California, considerable variations in retrieved fire area, occasionally by more than 50%, are observed when comparing the mid-latitude summer climatology and observation-based atmospheric profiles that are used in the sub-pixel retrieval algorithm. While regions of dry, brown vegetation may also increase the potential for error via the surface emissivity assumption, the algorithm is much more sensitive to errors in 11 μm background brightness temperature, where an error of only 1.0 K may alter the retrieved fire area by an order of magnitude or more. An independent application, using the Texas wildfire event of September 2011, reveals that the sub-pixel retrieval can even become irrelevant for 17.6% of the available MODIS fire pixels as a result of noise in the background region causing the 11 μm background brightness temperature to become warmer than the fire pixel, especially during daytime scenes. The various sources of uncertainty in the estimates of FRP_f and fire area can be reduced through the summation of individual pixel-level retrievals for large clusters of fire pixels, which can be defined based on the resolution of a mesoscale model grid. In comparison to the standard MODIS pixel-based FRP, the flux of FRP_f, defined as total FRP_f divided by the retrieved fire area, is shown to have a stronger and statistically significant correlation with surface (10-meter) wind speed and air temperature, especially for large fire pixel clusters, where the respective linear correlation coefficients are 0.55 and 0.77. These strong relationships suggest that, while additional studies are warranted, the flux of FRP_f may offer the potential for improved characterizations of the meteorological effects on fire intensity compared to the standard pixel-based FRP.

© 2012 Elsevier Inc. All rights reserved.

1. Introduction

Ignited by natural and anthropogenic causes (Koren et al., 2007; Peterson et al., 2010; van der Werf et al., 2008), global wildfire activity subsequently burns large tracts of land, releases aerosols and trace gases into the atmosphere, and can even have impacts on the global climate (Jordan et al., 2008; Kopacz et al., 2011; Randerson et al., 2006; Roy et al. 2008; Spracklen et al., 2007). Over the past three decades, several satellite sensors have been developed to provide the locations of

these wildfires at various spatiotemporal frequencies. For example, the MODerate Resolution Imaging Spectroradiometer (MODIS), located aboard the Terra (launched in 1999) and Aqua (launched in 2002) satellites, allows wildfires to be observed globally up to four times each day; twice in the daytime and twice at night. In contrast to other satellite sensors with fire monitoring capabilities, such as the NOAA Advanced Very High Radiometer (AVHRR), Geostationary Orbiting Environmental Satellite (GOES), and the Advanced Spaceborne Thermal Emission and Reflection Radiometer (ASTER), the MODIS sensor has a higher saturation temperature (~180 K higher) of ~500 K at its 4 μm fire detection channel (Gao et al., 2007; Justice et al., 2002; Kelha et al., 2003), which allows the retrieval of smaller fires and fire radiative power (FRP) — a quantitative measure of fire intensity (Kaufman et al., 1998a).

In recent years, the FRP data have provided a quantitative assessment of fire intensity across the globe (Ichoku et al., 2008a). Several studies

* Corresponding author at: University of Nebraska—Lincoln, Department of Earth and Atmospheric Sciences, 130 Bessey Hall, Lincoln, NE 68588, USA. Tel.: +1 219 742 261.

E-mail addresses: david.peterson@huskers.unl.edu (D. Peterson), jwang7@unl.edu (J. Wang).

have also shown that FRP is proportional to the fire's fuel consumption and smoke emission rates (e.g. Ichoku and Kaufman 2005; Ichoku et al., 2008a, 2008b; Jordan et al., 2008; Roberts et al., 2005, 2009; Wooster, 2002; Wooster et al., 2003, 2005). As a result, fires with a high FRP may produce higher altitude smoke plumes and a greater chance of smoke transport into the free troposphere (Val Martin et al., 2010). Above the boundary layer, smoke particles can be transported thousands of miles (e.g. Damoah et al., 2006; Duck et al., 2007; Sapkota et al., 2005; Westphal and Toon, 1991) creating health concerns and interacting with meteorological processes a great distance from a fire (e.g. Wang et al., 2006; Wang et al., in press). As a result, MODIS FRP data are being used for near real-time emission maps at a global scale (Kaiser et al., 2009) and may prove valuable for modeling smoke emissions at a relatively large model grid resolution (e.g. Wang et al., 2006). The primary limitation of the current MODIS FRP data is that they are estimates of fire radiative power released over a pixel area (FRP_p). In reality, any measurement of FRP is dependent on the sub-pixel fire area and fire temperature (e.g. Kaufman et al., 1998a), which can be highly variable from pixel-to-pixel (Peterson et al., in press). Therefore, a sub-pixel-based FRP calculation (FRP_f, derived from the retrieved fire size and temperature) could be a valuable asset to global fire monitoring (e.g. Peterson et al., in press; Zhukov et al., 2006) by providing estimates of the radiant energy (over the retrieved fire area) that in turn, produces the thermal buoyancy needed to inject smoke into the free troposphere (Kahn et al., 2007; Lavoue et al., 2000).

Prior to the calculation of FRP_f, the sub-pixel fire area and temperature must be retrieved, which is commonly accomplished via a bi-spectral approach (Dozier, 1981; Matson and Dozier, 1981; Flannigan and Vonder Haar, 1986; Prins and Menzel, 1992; Langaas, 1993; Peterson et al., in press) or a multispectral approach (Dennison et al., 2006; Eckmann et al., 2008, 2009, 2010). The bi-spectral approach takes advantage of the spectral contrast between a sub-pixel fire hot spot and the surrounding (presumably uniform) background of the pixel in the middle infrared (MIR, 4 μm) and thermal infrared (TIR, 11 μm) channels while the multispectral approach uses the radiances at multiple channels to disentangle the area fraction of many sub-pixel features (called endmembers), provided the number of endmembers is finite. Regardless of the methodology, a variety of variables may produce errors in the retrieved fire area and temperature, such as band-to-band point-spread function (PSF) coregistration issues, improper selection of background temperature and atmospheric transmittance, instrument noise, varying sub-pixel proportions of flaming, smoldering, and unburned areas, the solar contribution to the MIR, and the variation of surface emissivity between MIR and TIR (e.g. Giglio and Justice, 2003; Giglio and Kendall, 2001; Shephard and Kennelly, 2003). Validations of sub-pixel retrievals are difficult due to the need for high-resolution data that are coincident in time and space with observation of the satellite sensor. As a result of these limitations, sub-pixel retrievals have been used sparingly over the past three decades, aside from those developed by Prins and Menzel (1992, 1994) for the Geostationary Operational Environmental Satellite (GOES). However, the coarser resolution provided by the geostationary satellite sensor reduces the sensitivity to wildfires, making it difficult to use FRP_f from GOES quantitatively.

In the first of this series of two papers (Peterson et al., in press), a modified sub-pixel retrieval was developed to account for atmospheric effects and variations in Earth-satellite geometry for MODIS fire pixels, with the goal of application to future satellite sensors (e.g. VIIRS and GOES-R). The near-coincident observations obtained from the Autonomous Modular Sensor (AMS), flown aboard the NASA Ikhana unmanned aircraft, allowed the retrieved MODIS fire areas to be assessed with unprecedented accuracy (3–50 meter resolution). In addition, comparisons between the AMS and MODIS fire areas revealed the impacts from several indirect effects on the retrieval that are difficult to characterize, such as PSF effects, location relative to nadir (viewing zenith angle), and the overall distribution of sub-pixel hot spots within the fire pixel. As a result, it was suggested that a clustering methodology should be implemented

to reduce the error potential in retrieved fire area. These fire clusters, along with the sub-pixel-based FRP_f, allowed a large fire burning at a low intensity to be separated from a small fire burning at a high intensity and also facilitated calculations of FRP_f flux over the retrieved fire area.

Since the algorithm development and initial assessment have been presented by Peterson et al. (in press), this study focuses on the uncertainty introduced to the sub-pixel retrieval algorithm from errors in the estimated or assumed values of three primary direct input variables: (1) background brightness temperature, (2) background emissivity, and (3) the atmospheric column water vapor amount. Several earlier studies (e.g. Giglio and Kendall, 2001; Zhukov et al., 2006) have shown that temperature variations (noise) within the background region, especially at 11 μm, have the potential to dramatically affect the output of a sub-pixel retrieval. However, the potential impact resulting from an improper assumption of background emissivity or the atmospheric column water vapor amount (used for atmospheric correction) has not been quantitatively analyzed, and is paramount to understanding the overall sensitivity of this sub-pixel retrieval. With the recent aid of high-resolution AMS observations, deviations in retrieved fire area resulting from errors in these direct input variables and the subsequent effects on FRP_f and FRP_f flux can be assessed in great detail. Therefore, this paper builds upon earlier sub-pixel sensitivity studies by providing a detailed quantitative assessment of the current retrieval's sensitivity to error sources (1)–(3) via the California test cases used in Peterson et al. (in press). To complete the study, an operational version of our MODIS sub-pixel algorithm is applied to an independent, large wildfire event, allowing the overall performance, limitations, and utility of the retrieval to be further explored and assessed.

2. Data, study region, and the MODIS sub-pixel retrieval algorithm

This study incorporates the same California test cases (displayed in Fig. 1) and AMS data as Peterson et al. (in press), which also provides a detailed description of the sub-pixel algorithm development and assessment procedure, including a history of previous methodologies. For completeness, the following sections provide only a brief summary of this methodology. Section 7 describes the additional modifications that are required for operational purposes in the context of an independent case study of Texas and Oklahoma fire events during September 2011.

2.1. Data and study region

The MODIS sub-pixel retrieval requires the integrated use of the following three data products, either from MODIS/Terra or MODIS/Aqua, at a spatial resolution of 1 km² at nadir: (1) level 1B radiance data (MOD021KM/MYD021KM), (2) geolocation data (MOD03/MYD03), and (3) level 2, collection 5 fire product data (MOD14/MYD14). Data sources (1) and (2) are used to provide the radiance of the entire pixel and all relevant geometry information, such as solar zenith (SZA), relative azimuth (RAZ) and viewing zenith (VZA) angles (e.g. Wolfe et al., 2002), while the fire product (3) provides information on fire locations, 4 and 11 μm background temperatures, and FRP_p (Giglio et al., 2003; Justice et al., 2002; Kaufman et al., 1998a). The sub-pixel retrieval is only applied to the pixels that are flagged as fire pixels by the standard MODIS fire product, and is therefore subject to any limitations from the MODIS fire detection algorithm. For example, reasonable fire detections are only possible when the sub-pixel fire size is greater than ~100 m² (Giglio et al., 2003) and the FRP_p detection limits are about 9 and 11 MW for Terra and Aqua, respectively (Schroeder et al., 2010).

The AMS, flown aboard the NASA Ikhana Unmanned Airborne System (UAS), provides the high-resolution assessment data, which can vary in spatial resolution from 5 to 50 m due to changes in the platform altitude and the user-selectable field of view. The AMS has 12 spectral channels in the visible through thermal-infrared (Ambrosia and Wegener, 2009; Ambrosia et al., 2011a, 2011b). While several studies provide the
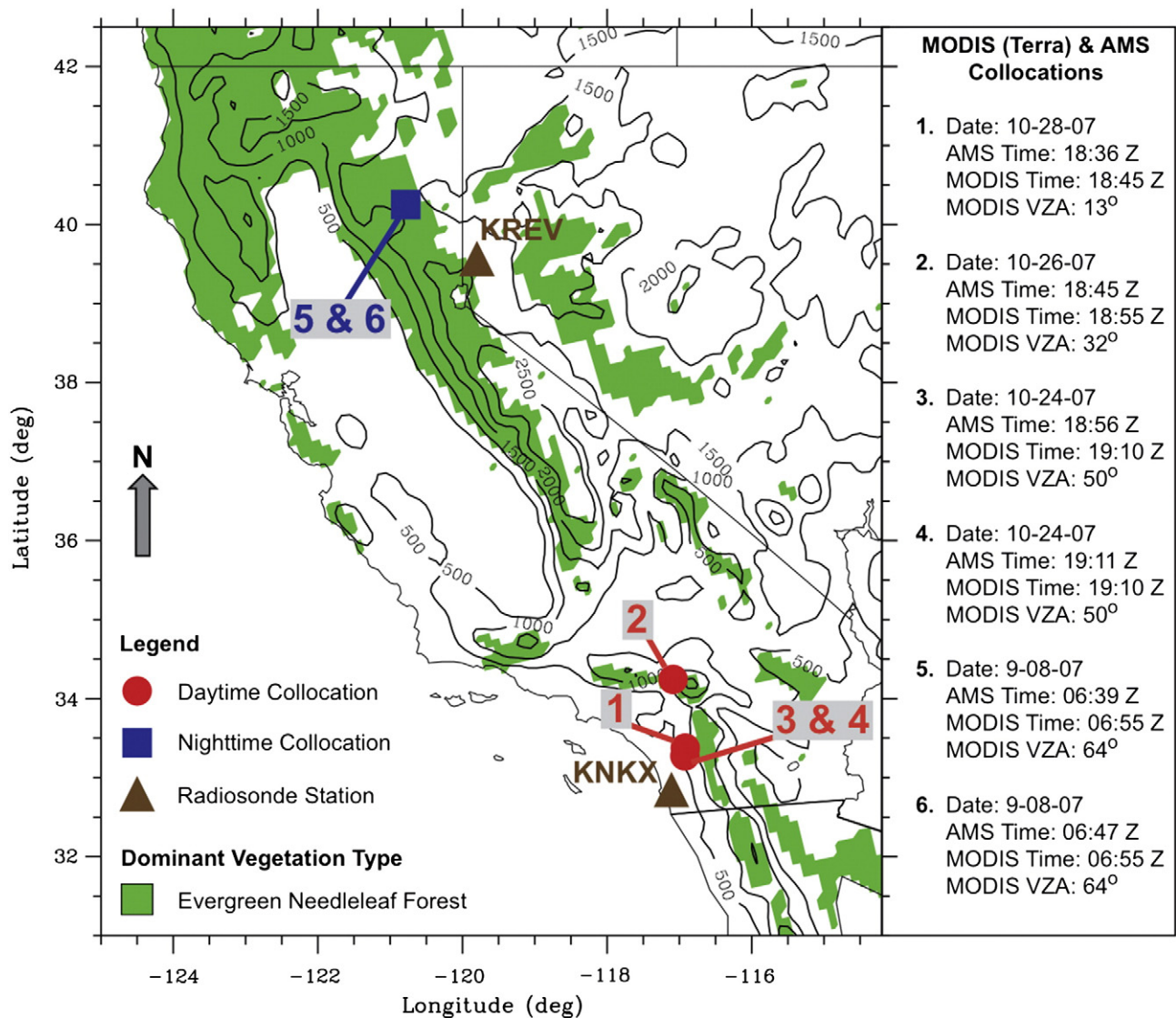
Fig. 1. Map showing the locations of the six California test cases as red circles (daytime) or a blue box (nighttime). The specifics of each MODIS and AMS collocation are provided in the side panel, with the viewing zenith angle (VZA) corresponding to the mean VZA for all MODIS fire pixels in each test case. Green shading indicates regions where evergreen, needle-leaf forest is the dominant vegetation type and black contours indicate variations in topography, with a contour interval of 500 m. In addition, the locations of the two relevant radiosonde stations are displayed as brown triangles (see Section 3.1 for details). (For interpretation of the references to color in this figure legend, the reader is referred to the web version of this article.)

theoretical basis for a general AMS fire detection algorithm (Cahoon, et al., 1992; Flasse and Ceccato, 1996; Li et al. 2000a, 2000b), Peterson et al. (in press) developed a separate algorithm specifically designed to use the AMS 3.75 μm and 10.76 μm channels to separate the regions of actively burning fires from the remaining data points (including smoldering and cooling) within the boundaries of any MODIS fire pixel. The AMS generally provides 4000 to 9000 data points per MODIS fire pixel, thus producing a detailed representation of MODIS sub-pixel fire properties. However, the smoldering region is largely neglected because the AMS data used in this study were collected for very intense fire events in California, and the sub-pixel calculation is likely weighted toward retrieving the flaming region (largest contribution to pixel MIR radiance).

Similar to MODIS, the AMS fire detection algorithm is threshold-based. However, modifications are required to overcome the unique challenges encountered from changes in the AMS flight altitude and surface topography, which can affect the background temperature and cause variations in the fire detection thresholds (Peterson et al., in press). As a result, the background temperature selection criteria and fire detection thresholds used in AMS fire assessment algorithm by Peterson et al. (in press) are image-based, and allowed to vary within the boundaries of each MODIS fire pixel. While the AMS reliably measures brightness

temperature at 11 μm, the 4 μm channel saturates at high brightness temperatures (510–530 K). The AMS fire assessment algorithm assumes that any data at the saturation level are hot enough to be considered as fire, but the remainder of the data below the saturation level must also be examined. Therefore, the AMS fire detection thresholds are set at a region of low density that separates the flaming region from the remaining data in the 4 and 11 μm histograms (Peterson et al., in press). The areas of the individual AMS pixels with a temperature greater than the 4 and 11 μm fire thresholds are then summed to calculate the fire hot spot area within the MODIS pixel under consideration (assessment data). With the saturation limit in the 4 μm channel precluding any fire temperature or FRP investigations, the AMS fire assessment algorithm is primarily used for fire area and background temperature information.

The temporal difference between AMS and MODIS is limited to a maximum of 16 min before or after the MODIS overpass to ensure that MODIS and AMS are observing the same fire characteristics, near-simultaneously. With this collocation criterion, a total of six AMS flight data scans from August to October 2007, including single and multiple fires, are available for a fire event in Northeastern California and a Santa Ana driven event in Southern California (Peterson et al., in press). The Ikhana commonly flies over the same fire event multiple times on adjacent, short-duration (3–

5 min) flight tracks, occasionally allowing a single MODIS scene to provide two collocations (e.g. test cases #3 and #4 in Fig. 1). In addition, Fig. 1 shows that all six of these California test cases are located in forested regions with complex topographic features.

2.2. MODIS sub-pixel retrieval algorithm

The FRP_f calculation is based on a modified, bi-spectral retrieval of sub-pixel fire area and temperature (Peterson et al., in press). Prior to the calculation step, output from the Santa Barbara DISORT Atmospheric Radiative Transfer (SBDART) model is used to correct the observed radiances at 4 and 11 μm for atmospheric and solar effects. SBDART calculates the radiative transfer from the ultraviolet through the infrared wavelengths (Ricchiazzi et al., 1998), and can simulate the top-of-atmosphere (TOA) radiance as a function of fire area fraction (P, where $0<P<1$) and fire temperature (T_f). When applying SBDART to the MODIS sub-pixel retrieval, the observed radiances at 4 and 11 μm, denoted by L_4 and L_{11}, respectively, are

$$L_4 = \tau_4 PB(\lambda_4, T_f) + (1-P)L_{4b} \tag{1}$$

$$L_{11} = \tau_{11} PB(\lambda_{11}, T_f) + (1-P)L_{11b} \tag{2}$$

where $B(\lambda,T)$ is the Planck function, τ_4 and τ_{11}, respectively denote the upward MIR atmospheric transmittance and the upward TIR atmospheric transmittance, and the background radiances at the TOA, denoted by L_{4b} and L_{11b}, are a function of several variables expressed respectively, as

$$L_{4b} = \tau_4[e_{4b}B(\lambda_4, T_b) + (1-e_{4b})I_{4ref}] \tag{3}$$

$$L_{11b} = \tau_{11}e_{11b}B(\lambda_{11}, T_b) \tag{4}$$

where e_{4b} and e_{11b}, respectively denote the assumed background emissivity, I_{4ref} is the reflected solar radiance in the 4 μm channel at the surface (equal to zero at night), and T_b is the surface kinetic background temperature (Dozier, 1981; Peterson et al., in press; Prins and Menzel, 1992). The emissivity of the fire is commonly assumed to be equal to one (e.g. Giglio and Kendall, 2001), which has been shown to be a reasonable assumption for most fire events with thick fire fronts. Therefore, Eqs. (1) and (2) do not include emissivity in the fire term.

By combining Eqs. (1)–(4), SBDART is run repeatedly for various sets of the possible geometry values, T_f, and P, and the output TOA radiances are saved together with the input parameters as a lookup table for 4 and 11 μm. Additional key entries in the lookup tables include various sets of L_{4b} and L_{11b}, which can be used in place of T_b, e_{4b} and e_{11b} (Eqs. (3) and (4)) because the MODIS fire detection algorithm, under the assumption of identical surface and atmospheric conditions, provides an estimate of the TOA brightness temperature for the surrounding fire-free (background) pixels that can be used to directly compute L_{4b} and L_{11b} (Giglio, 2010; Giglio et al., 2003). Therefore, for any given MODIS fire pixel, T_f and P can be extracted from the lookup tables by matching the viewing geometries, incorporating L_{4b} and L_{11b} as entries, and using L_4 and L_{11} as constraints. The actual retrieval implements a multistep, iterative process (e.g. Shephard and Kennelly, 2003) to aid in solving Eqs. (1) and (2) for each MODIS fire pixel in any given scene (Peterson et al., in press). It is worth noting that while the MODIS fire product provides an estimate of L_{4b} and L_{11b}, the simulation of TOA radiance in the lookup tables requires the consideration of emissivity and atmospheric effects (e.g. τ_4 and τ_{11}) to ensure physical consistence in Eqs. (1)–(4). As a result, the retrieval may be sensitive to these parameters.

Following the retrieval of fire area and temperature, FRP_f is calculated (units of Megawatts, above the mean background) via the Stefan–Boltzmann relationship in the 4 μm channel

$$FRP_f = \sigma\left(T_f^4 - T_{4b}^4\right)A_f \tag{5}$$

where σ is the Stefan–Boltzmann constant (5.6704×10^{-8} W m^{-2} K^{-4}), T_f is the retrieved kinetic fire temperature at the surface (not the pixel temperature), A_f is the retrieved fire area, and T_{4b} is the 4 μm background brightness temperature, which can be used as an approximation of surface kinetic background temperature because atmospheric effects, especially from the column water vapor amount, are minor at cool 4 μm temperatures (see Section 3). In contrast, the current MODIS FRP_p is based on a best-fit curve for thousands of simulated sub-pixel fire scenarios, given by

$$FRP_p = 4.34\times10^{-19}\left(T_4^8 - T_{4b}^8\right)A_p \tag{6}$$

where T_4 is the pixel brightness temperature and A_p is the area of the fire pixel (Giglio, 2010; Giglio et al., 2003; Kaufman et al., 1998a, 1998b, 2003). Peterson et al. (in press) show that these two pixel-level methods are strongly related. However, FRP_f may provide improved results for off-nadir pixels due to the consideration of atmospheric effects, Earth-sensor geometry, and the characteristics of each individual fire (other than using a best fit methodology, such as Eq. 6).

In addition to the pixel-level FRP_f retrievals, a clustering methodology is implemented to reduce the potential for large, somewhat random errors, such as inter-channel PSF effects and instrument noise (e.g. Peterson et al., in press; Wooster et al., 2003; Zhukov et al., 2005, 2006). For simplicity, a general summation method can be used, where each individual (pixel-level) retrieved fire area and FRP_f is summed to obtain the area and FRP_f of an entire fire event. Fire pixel clustering also allows the FRP fluxes to be calculated by

$$FRP_f \ flux = \frac{\sum\limits_{i=1}^{n} FRP_{f_i}}{\sum\limits_{i=1}^{n} A_{f_i}} \tag{7}$$

$$FRP_p \ flux = \frac{\sum\limits_{i=1}^{n} FRP_{p_i}}{\sum\limits_{i=1}^{n} A_{p_i}} \tag{8}$$

where the output is provided in units of W m^{-2} per fire pixel cluster (Peterson et al., in press). While the FRP_p flux is limited to the total area of the fire pixel cluster, the FRP_f flux provides a fire size-based representation of FRP that can be used in combination with retrieved fire cluster area to aid in discerning the fire characteristics of any given event (e.g. a large fire burning at a low intensity).

When calculating FRP_f flux per individual fire pixel, the large uncertainty produced by indirect effects is further augmented by the cancelation of the fire area term (Eq. 7) because the offset in error between retrieved fire area and temperature no longer exists (e.g. Zhukov et al., 2006, also described in the following section). Therefore, the utility of FRP_f flux in the fine-scale modeling of individual fires and smoke plumes may be compromised. In contrast, mesoscale and global modeling, one of the primary applications for MODIS fire data, uses a grid mesh to cover several fires (e.g. Wang et al., 2006; Wang et al., in press), and requires the averaged energy over the total fire area to estimate smoke plume buoyancy. The calculation of FRP_f flux (Eq. 7) meets this requirement, and is therefore the primary motivation for using the sub-pixel retrieval. While fire pixel clustering alleviates many of the indirect sources of error, such as PSF effects (Peterson et al., in press), the assumption of the atmospheric profile and background emissivity (e.g. Eqs. (3) and (4)), as well as inherent errors from the MODIS fire product background brightness temperature undoubtedly impact the accuracy of the sub-pixel retrieval and the subsequent calculation of FRP_f flux. Therefore, Sections 3, 4, and 5 are respectively devoted to quantifying the sub-pixel retrieval's uncertainty associated with these variables and assumptions.

3. Atmospheric profile

Considering that the AMS fire data used in this study are for California fire events occurring in the late summer or early fall (Fig. 1), the atmospheric profile in SBDART is assumed to be a representative, climatologically based mid-latitude summer profile (default profile) for the Continental United States, which includes 2.92 g/cm^2 of water vapor in the atmospheric column (McClatchey et al. 1972; Ricchiazzi et al., 1998). However, the day-to-day relative change of water vapor will likely have an effect on the retrieval. Therefore, the sensitivity of the 4 and 11 μm channels to water vapor amount must be examined.

3.1. Variations in water vapor amount and temperature

As shown by Kaufman et al. (1998a), water vapor absorption is minimal in the primary (3.96 μm) MODIS fire detection channel, but its impact at 11 μm is less certain. Fig. 2a and b is based on the water vapor amount and show comparisons between the surface kinetic temperature (T_{sfc}) and the top-of-atmosphere (TOA) brightness temperature (BT_{TOA}) for a test case near nadir (case #1, mean VZA = 13°) and a test case at the edge of a given scene (cases #5 and #6, mean VZA = 64°). From this display, it is immediately evident that an atmospheric correction is required for the 11 μm channel, evidenced by 11 μm BT_{TOA} values that are at least 100 K cooler than T_{sfc} (when $T_{sfc} > \sim 700$ K), especially when the VZA is 64° (longer path length). At the 4 μm background BT_{TOA} range, commonly 290–315 K, the difference between T_{sfc} and BT_{TOA} is very small (<10 K), and is the primary reason for not correcting the MODIS 4 μm background temperature (T_{4b}) in Eq. (5). However, an atmospheric correction does become necessary as the 4 μm surface temperature increases (presumably from fire) because the relative change between T_{sfc} and BT_{TOA} remains approximately the same. For example, a T_{sfc} of 400 K will produce a 4 μm BT_{TOA} that is ~8 K (16 K) cooler when the VZA is 13° (64°), but this change grows to ~80 K (160 K) when the surface temperature warms to 1400 K.

The deviations in BT_{TOA} relative to the values obtained in Fig. 2a and b are displayed in Fig. 2c–f as a function of T_{sfc} and several potential column water vapor amounts. At 4 μm (Fig. 2c and e), a large increase or decrease in column water vapor (from the mid-latitude summer value) will produce small changes in BT_{TOA}, falling within the ranges of ± 14 K and ± 26 K when the VZA is respectively 13° and 64°, for any given T_{sfc} value. In contrast, the steep slope and tight gradient of the contours in Fig. 2d and f shows that the 11 μm BT_{TOA} is much more sensitive to small changes in column water vapor than 4 μm, especially when T_{sfc} is high (e.g. >1000 K). In these cases, the 11 μm BT_{TOA} can change by more than ± 100 K. The impact of water vapor absorption is even more significant at the VZA of 64° (Fig. 2f), where deviations in BT_{TOA} of more than ± 200 K can occur for relatively small changes in column water vapor amount, especially for high values of T_{sfc}.

The larger impact of column water vapor amount on the 11 μm BT_{TOA} partially results from a relatively large reduction in atmospheric transmission (as compared to the counterparts at 4 μm). For example, the mid-latitude summer water vapor profile (2.92 g/cm^2) produces a transmissivity of about 0.96 and 0.87 at 4 and 11 μm, respectively. However, a modified profile, containing 1.1 g/cm^2 of column water vapor, produces 4 and 11 μm transmissivities of 0.98 (2% change) and 0.93 (7% change), respectively. In addition, the BT_{TOA} of a fire pixel may increase relatively less at 11 μm when compared to 4 μm because the wavelength of peak emission shifts toward shorter wavelengths as the temperature increases (e.g. Wein's Law). Therefore, the combination of increased water vapor absorption and lower sensitivity to warm temperatures likely explains the large surface to TOA temperature differences observed at 11 μm in Fig. 2d and f, which may ultimately affect the accuracy of the bi-spectral, sub-pixel retrieval.

In many California fire events, the atmospheric water vapor amount will be low, especially near the surface, ultimately resulting in a lower column water vapor amount than the mid-latitude summer profile. In fact, most of the test cases are associated with a Santa Ana synoptic pattern and cloud cover effects are minor, even in the northern California test cases (#5 and #6). MODIS level-2 water vapor data (MOD05_L2/ MYD05_L2, King et al., 2003) show that the column water vapor in the vicinity of the six test cases ranges from about 0.75 to 1.70 g/cm^2, which is a considerable deviation from the mid-latitude summer value of 2.92 g/cm^2 and falls near the minimum value considered in Fig. 2c– f. Any impacts from variations in the temperature profile are also uncertain.

Based on the potential for large, regional deviations in the atmospheric profiles, a mean observed sounding from all six test cases was derived and compared to the mid-latitude summer SBDART profile. For the southern California test cases (#1–4 in Fig. 1), observed soundings were obtained from San Diego, California (station KNKX, #72293), while Reno, Nevada (station KREV, #72489) was used for the Northern California test cases (#5–6 in Fig. 1). With the MODIS overpass occurring near the midpoint between the 12:00 Z (day 1) and 00:00 Z (day 2) sounding times for test cases #1–4 (between 00:00 Z and 12:00 Z on day1 for test cases #5–6), the sounding at the time of the MODIS overpass is simply the mean of the a priori and a posteriori soundings. The observed atmospheric profile (to be compared with the mid-latitude summer profile) can then be produced by calculating median of the four mean water vapor and temperature profiles coincident with the four MODIS overpasses. Fig. 3a and b shows that the mid-latitude summer temperature profile falls within the observed range of temperature at many levels, but deviates by 2–5 K near the surface (inversion effects) and by 10 K near the tropopause.

The observed profile is computed using only the mandatory pressure levels, which are subsequently interpolated to the levels of the SBDART input sounding. As a result, the column water vapor amount is fairly strict and may change if more levels were considered or if the local sounding observation times were closer to the MODIS overpass times. For example, the total column water amount of the observed profile ranges from 0.59 to 1.35 g/cm^2, which is lower than the range of 0.75 to 1.70 g/cm^2 provided by MODIS water vapor data. However, both techniques show there is a considerable deviation from the mid-latitude summer value, resulting from reduced mixing ratios in the lowest 75% of the sounding (Fig. 3c and d). A large range in mixing ratio values also exists below 5 km due to the potential for marine influences (e.g. afternoon sea breeze), primarily from test cases #1–4, impinging on these otherwise dry regions of the western United States. However, the observed range commonly falls below the mid-latitude summer values and suggests that uncertainty may be introduced in the sub-pixel retrieval, primarily from the increased 11 μm transmissivity.

3.2. Retrieval uncertainty associated with the atmospheric profile

While earlier studies on sub-pixel retrievals did incorporate an atmospheric correction (e.g. Giglio and Kendall, 2001; Zhukov et al., 2005, 2006), few, if any, of these studies show the effects originating from an improper assumption of the atmospheric profile. In this study, modified 4 and 11 μm lookup tables were produced using the observed temperature and water vapor profiles described in the previous section, allowing the theoretical relationships between the 4 and 11 μm pixel temperature to be examined for each atmospheric profile. Specific examples are presented in Fig. 4a–d, corresponding to the sub-pixel retrieval's lookup table for a single fire pixel in test case #1 when the VZA = 14°, SZA = 48°, and RAZ = 165°. Each dashed curve represents the pixel temperatures at 4 and 11 μm that result from specified values of fire area fraction for varying fire temperatures. Each solid curve, on the other hand, represents the pixel temperatures that result from specified values of fire temperature for varying fire area fractions. From this display, it is immediately evident that the 4 μm channel is more sensitive to changes in fire temperature and the 11 μm channel is more sensitive to changes in fire area fraction. Therefore, drawing from the water vapor effects at 11 μm (Fig. 2d and f), changes in the atmospheric profile
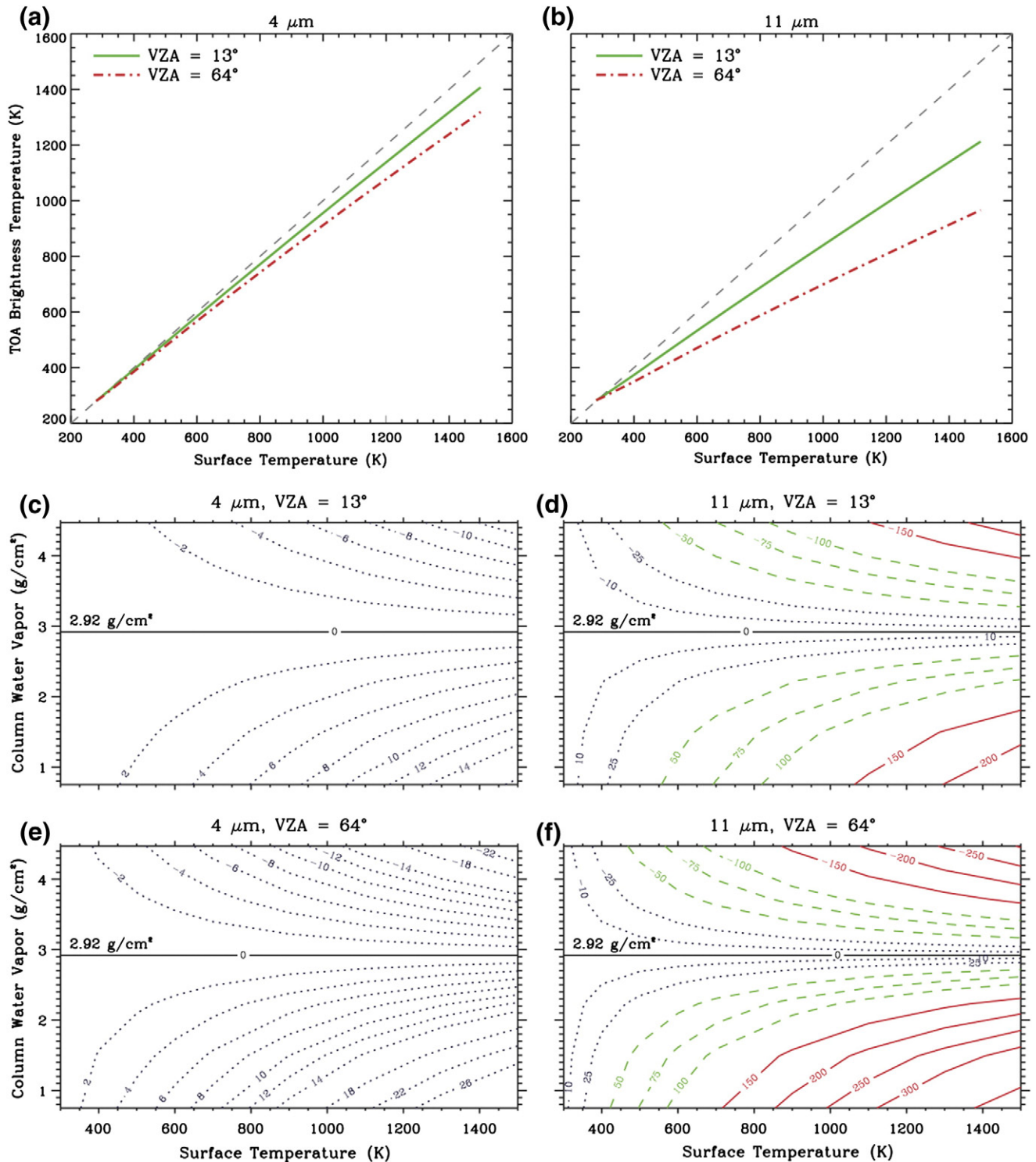
Fig. 2. Displays showing the sensitivity of the 4 and 11 μm channels to variations in atmospheric column water vapor amount for a case with a solar zenith angle of 48° and relative azimuth angle of 165°. (a) and (b) Comparisons between T_{sfc} and BT_{TOA} using the mid-latitude summer column water vapor amount (2.92 g/cm^2) for the 4 and 11 μm channels, respectively. VZAs of 13° and 64° are respectively denoted by the solid green and dashed red lines. (c)–(f) Contour plots showing the change in BT_{TOA} relative to the values obtained using the mid-latitude summer column water vapor amount as a function of T_{sfc} and column water vapor amount. The 4 and 11 μm channels are respectively displayed in (c) and (d) for the viewing zenith angle of 13°. Similarly, (e) and (f) correspond to the viewing zenith angle of 64°. The solid, black contour indicates the mid-latitude summer column water vapor amount and dotted blue, dashed green, and solid red contours indicate a positive (or negative) change in BT_{TOA} of <50 K (>−50 K), 50 to 149 K (−50 to −149 K), and ≥150 K (≤−150 K), respectively. (For interpretation of the references to color in this figure legend, the reader is referred to the web version of this article.)

are likely to have the largest impact on retrieved fire area because for the same fire area fraction and fire temperature, less water vapor will greatly increase the brightness temperature at 11 μm.

When comparing the retrieval that uses the mid-latitude summer atmospheric profile (Fig. 4a), with the retrieval that is modified for the observed atmospheric profile (Fig. 4c), the reduced column water vapor in the latter case renders a shift of the entire lookup table towards higher 11 μm brightness temperatures, with little change based on the 4 μm channel. Consequently, the primary impact on the retrieval is a reduction in fire area fraction (between Fig. 4a and c) for any given set of
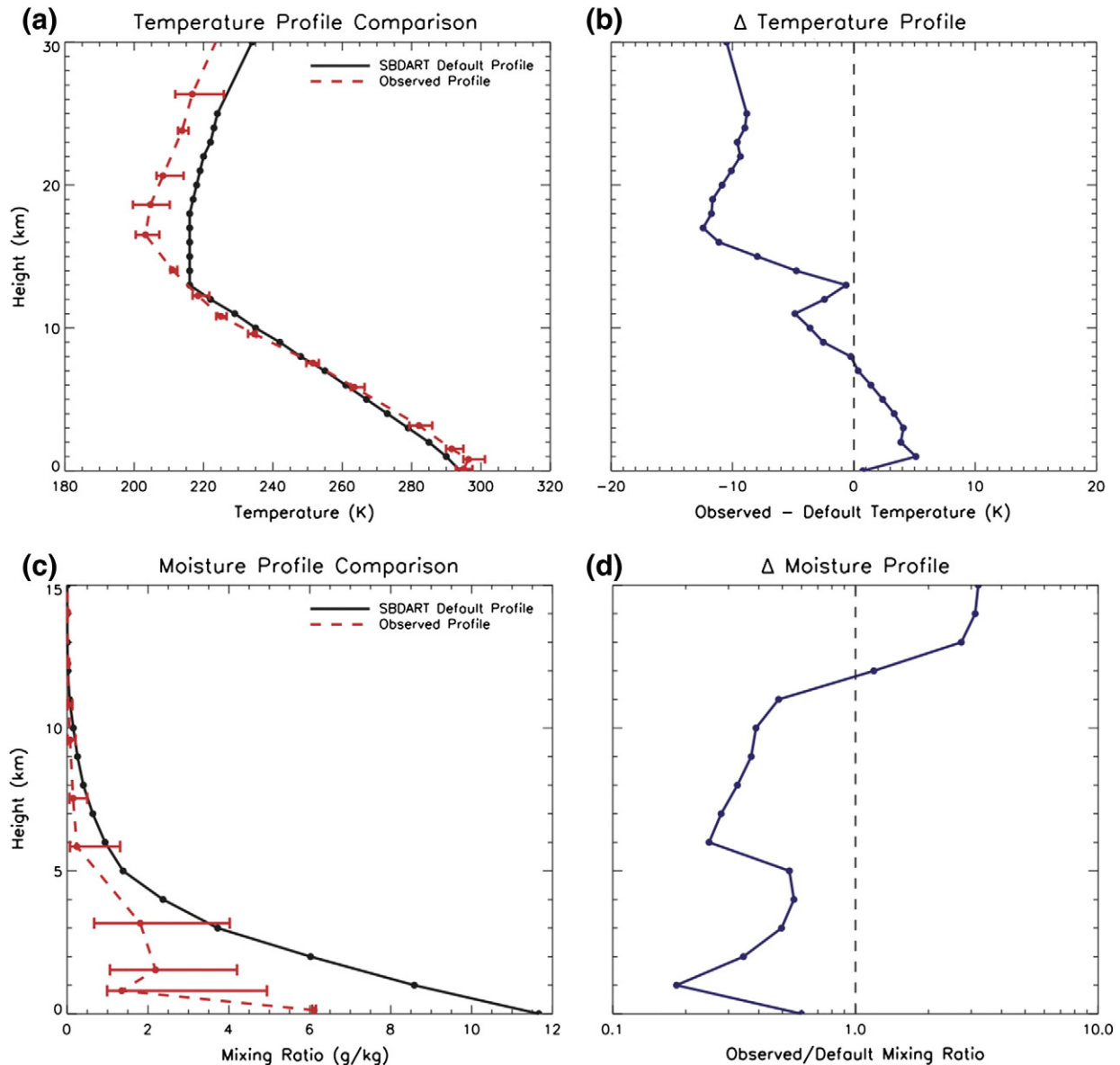
Fig. 3. Atmospheric profile comparisons. (a) Comparison between the observed (dashed red) and the default mid-latitude summer (solid black) temperature profiles. Red error bars indicate the range of observed temperatures at each height AGL, with each red data point corresponding to the median. (b) The observed temperature profile (interpolated to match the height levels of the default mid-latitude summer profile) subtracted from the default profile (absolute change). (c) and (d) Same as (a) and (b), respectively, but for the moisture profiles (mixing ratio), with the relative change (observed/default) in mixing ratio used in (d). (For interpretation of the references to color in this figure legend, the reader is referred to the web version of this article.)

pixel temperatures. However, the retrieved fire temperature concurrently increases (to a lesser extent) due to the minimal atmospheric effects at 4 μm. The superimposed red dot displayed in Fig. 4b and d (corresponding to the location in Fig. 4a and c) represents the actual retrieval result (described in Section 2.2) and highlights the effect caused by a change in the atmospheric profile. This sample fire pixel has an observed 4 μm pixel temperature of 366.8 K and 11 μm pixel temperature of 306.3 K, which produces a retrieved fire area fraction of 0.012 and a fire temperature of 660 K using the mid-latitude summer lookup tables. In contrast, the fire area fraction decreases to 0.007 and the fire temperature increases to 720 K when using the modified lookup tables.

Similar to Fig. 4, the retrieved fire area for all 33 valid fire pixels (from test cases #1 to #6) is overestimated when using the mid-latitude summer atmospheric profile (red data points in Fig. 5a) compared to the observed profile (blue data points in Fig. 5a), with a mean difference of 69.1%. Fig. 5a also shows that this overestimation is slightly larger for the fire pixels with large VZAs, which can be explained by the effect of longer path lengths (displayed in Fig. 2e and f). Interestingly, the

modified retrieval for the observed atmospheric profile does not improve the correlation between the retrieved fire area and the AMS observations (R=0.57) when compared to the counterparts from using the mid-latitude summer profile (R=0.59, Table 1). In fact, the observed profile seems to result in retrieved fire areas that may even be too low compared to AMS, which likely stems from the low column water vapor amount value of 1.06 g/cm^2. Fig. 2c–f shows that a column water vapor observation of less than ~1.5 g/cm^2 falls in the region where the BT_{TOA} changes rapidly for small changes in water vapor amount. Therefore, relatively small errors in the water vapor profile will result in a relatively large change in retrieved fire area.

As a result of the offsetting changes in fire area fraction and temperature (Fig. 4) from the observed profile, it can be expected that the effect on FRP_f (Eq. 5) will be relatively small in comparison to fire area. Fig. 5b incorporates the current MODIS FRP_p (Eq. 6) as a base for comparison, and shows that the change in FRP_f is indeed small, with a mean 20.7% and many pixels less than 10%. As with fire area, the largest differences occur with large VZAs, but also at high FRP values. In these cases, the
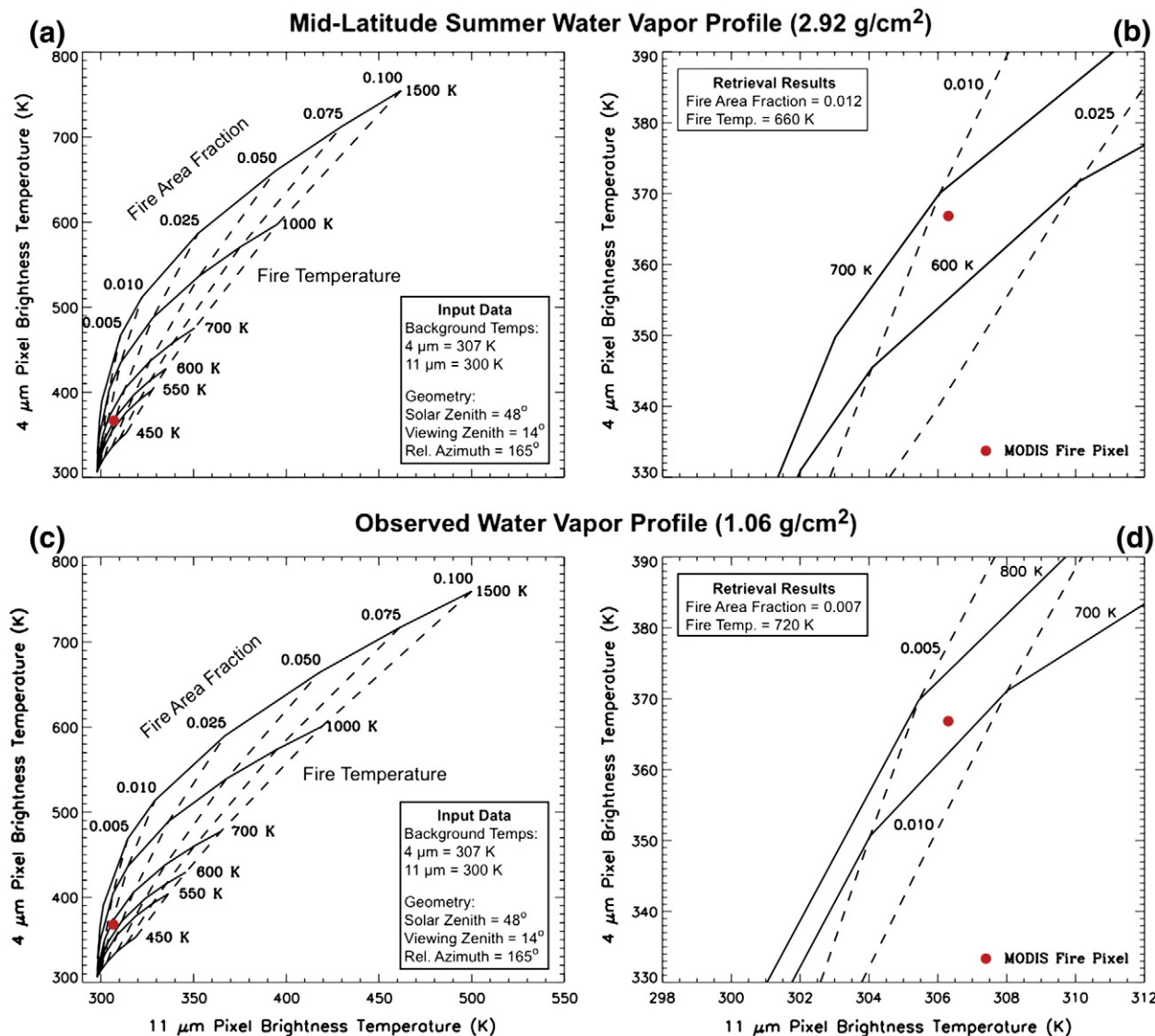
Fig. 4. Theoretical relationships between the 4 and 11 μm pixel temperature for various values of fire temperature and fire area fraction when using the input data for California test case #1 (displayed in Fig. 1). Panels (a) and (c) respectively show the lookup tables needed for the sub-pixel retrieval using the climatologically based mid-latitude summer water vapor profile (2.92 g/cm²) and the observed water vapor profile (1.06 g/cm²). Each dashed curve represents the relationship between the 4 and 11 μm pixel brightness temperatures at specified values of fire area fraction for varying fire temperatures. Each solid curve represents the relationship between the 4 and 11 μm pixel brightness temperatures at specified values of fire temperature for varying fire area fractions. Zoomed views of the lower-left portion of (a) and (c) are respectively displayed in (b) and (d), and correspond to the location of the superimposed red dot, which indicates a sample fire pixel from California test case #1. The specific retrieval inputs and results are provided in the black boxes.

surface fire temperature is likely larger, which would enhance the effect of an atmospheric correction based on Fig. 2. The observed profile also increases the correlation between FRP_p and FRP_f ($R = 0.98$) and reduces the RMSE by 59.4% (Table 1). However, caution must be used when interpreting this result because FRP_p itself is based on a best-fit methodology with its own uncertainty (e.g. Kaufman et al., 1998a), and detailed validations of FRP via the AMS (or any other sensor) are currently unavailable. Therefore, comparisons between FRP_f and FRP_p should be considered as an indirect quality check rather than a direct validation (Peterson et al., in press).

Regardless of the atmospheric profile, Fig. 5c highlights the larger and more realistic values of the FRP_f flux (3000–15,000 W m⁻², Eq. 7) in comparison to the FRP_p flux (20–80 W m⁻², Eq. 8), which serves as a reference point for the standard MODIS fire product (Peterson et al., in press). However, the FRP_f flux values produced using the observed profile are larger than their counterparts produced by the mid-latitude summer profile, with a mean difference of 53.2% (Fig. 5c). This stems from the large impact that variations in water vapor amount have on retrieved fire area (Fig. 5a and Table 2). As displayed in Fig. 5a, the lower column

water vapor amount in the observed profile will significantly reduce the retrieved fire area, which produces a smaller denominator in Eq. (7) and concurrently increases the cluster FRP_f flux. Therefore, an accurate selection of the atmospheric profile is essential for an accurate retrieval of cluster FRP_f flux, especially when the atmospheric column water vapor amount is very low. This study only provides one such example and other locations with very low (or very high) column water vapor amounts, as well as regions with large seasonal temperature variations (e.g. winter fire events) may also require a modified atmospheric profile. Therefore, if the retrieval is applied on a global-scale, a variety of atmospheric profiles will be included with the lookup table calculations.

4. Background emissivity

The 4 and 11 μm background emissivities (e_{4b} and e_{11b} in Eqs. (3) and (4)) are assumed to be respectively equal to 0.95 and 0.97 (e.g. Giglio et al., 1999; Petitcolin and Vermote, 2002; Tang et al., 2009), which is true for relatively dense, green vegetation, such as the temperate evergreen forests used in this study. However, vegetated surfaces with a higher
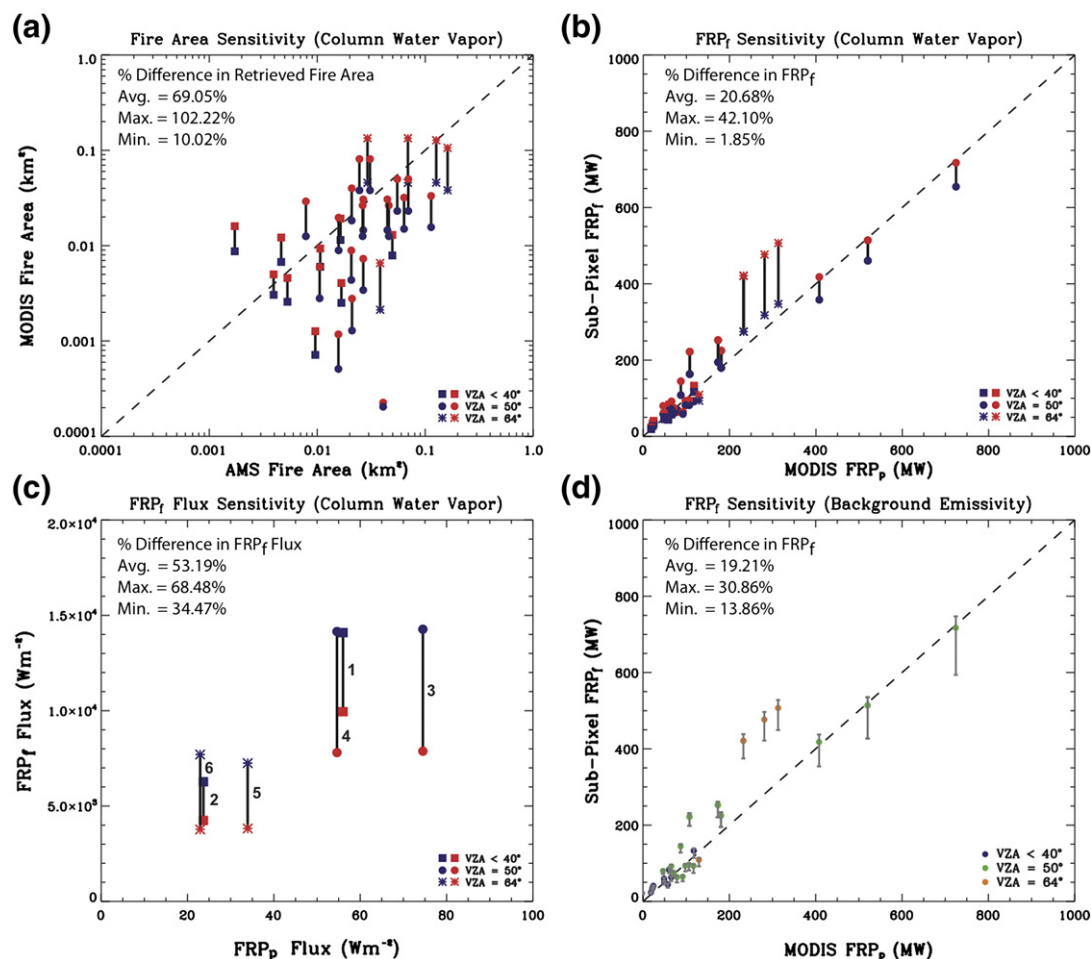
Fig. 5. Retrieval sensitivity to atmospheric column water vapor amount and background emissivity. (a) Pixel-level comparisons between retrieved MODIS fire area and AMS observed fire area, with black error bars indicating the change in retrieved fire area using the mid-latitude summer (red symbols) and the observed (blue symbols) water vapor profiles. (b) and (c) Same as (a), but respectively for pixel-level comparisons between FRP_p (MODIS pixel-based FRP) and FRP_f (sub-pixel-based FRP) and cluster-level comparisons between FRP_p per cluster pixel area (FRP_p flux) and FRP_f per fire area (FRP_f flux) using the sum of pixel-level retrievals method. The California test case labels in (c) correspond to Fig. 1. The plot symbol type in (a–c) indicates the viewing zenith angle of each pixel. (d) Same as (b), but gray error bars are used to indicate sensitivity to background emissivity selection for several green and brown vegetation scenarios, with the color scheme indicating the viewing zenith angle. (For interpretation of the references to color in this figure legend, the reader is referred to the web version of this article.)

reflectivity, such as dry grassland, may result in a large departure from the assumed values and may also result in a significant inter-channel difference. For example, Giglio et al. (1999) show that emissivities for dry savannah or dry temperate grasslands are about 0.86 and 0.92 at 4 and 11 μm, respectively.

In order to study how each region's background emissivity may affect the retrieval, the MODIS sub-pixel algorithm is run for each potential emissivity situation provided in the literature, ranging from 0.75–1.0 at 4 μm and 0.91–1.0 at 11 μm. For most pixels, the difference in retrieved fire area is between 6.2% and 25.3% with a mean of 11.3% (Table 2),

which corresponds to a change in fire area from less than 100 m² to over 1000 m². In addition, the potential variability in retrieved fire area is independent of the size of the fire event (based on AMS observations, not displayed). However, if the dry grass situations are removed, then the mean variability would decrease to ~3.4% and most pixels would fall in the range of 1% to 7%.

The effect of background emissivity on FRP_f and FRP_f flux is also small, but in contrast to the atmospheric profile sensitivity, FRP_f is actually the most sensitive output variable (Fig. 5d and Table 2) due to the larger range of potential emissivity values associated with the 4 μm channel. As shown in Fig. 4, the 4 μm channel is highly sensitive to changes in retrieved fire temperature, hence this dual channel emissivity simulation affects FRP_f slightly more than retrieved fire area, with a mean variability of 19.2%. Fig. 5d shows that this variability increases with increasing FRP_f, which is largely independent of the observed VZA. However, as with retrieved fire area, the sensitivity of FRP_f to background emissivity becomes almost negligible if the dry, brown vegetation scenarios are removed. Therefore, with the six test cases located in regions that are dominated by forest (Fig. 1), it is very likely that the assumed emissivity values (0.95 at 4 μm and 0.97 at 11 μm) will not result in large retrieval errors. In fact, regions that are completely dominated by dry, brown vegetation are the only situation where the emissivity impact would become significant. In these cases, emissivity

Table 1
Statistics for the atmospheric effect on retrieved fire area and FRP.

Column water vapor amount (g/cm²)	RMSE	R	R²
MODIS (retrieved) vs. AMS (observed) fire area (km²)			
2.92 (mid-latitude summer)	0.03	0.59	0.35
1.06 (observed)	0.04	0.57	0.32
Sub-pixel FRP_f vs. Current MODIS FRP_p (MW)			
2.92 (mid-latitude summer)	77.57	0.93	0.86
1.06 (observed)	31.5	0.98	0.96

Table 2
Sensitivity summary for the MODIS sub-pixel retrieval.

Variable	% change in variable		
33 MODIS fire pixels	Min.	Max.	Mean
Atmospheric profile (mid-latitude summer vs. observed)			
Retrieved fire area	10.02	102.22	69.05
FRP_f	1.85	42.1	20.68
Cluster FRP_f flux	34.47	68.48	53.19
Background emissivity (0.75–1.00)			
Retrieved fire area	6.22	25.27	11.29
FRP_f	13.86	30.86	19.21
Cluster FRP_f flux[a]	10.9	16.43	9.06
4 μm background temperature (±5.0 K from observation)			
Retrieved fire area	4.18	55.67	22.92
FRP_f	2.92	43.03	13.71
Cluster FRP_f flux[a]	14.09	36.56	20.78
11 μm background temperature (±1.0 K from observation)[b]			
Retrieved fire area	50.6	196.22	121.96
FRP_f	5.29	79.03	37.61
Cluster FRP_f flux[a]	93.68	131.44	104.95

[a] FRP_f flux sensitivity is based on the sensitivity to retrieved fire area.
[b] Background temperatures are not allowed to increase above the pixel temperature.

or NDVI data from MODIS (or other sources) could be incorporated as a direct input variable, which may prove valuable if the sub-pixel algorithm is implemented on a global-scale.

5. Background temperature

For any sub-pixel calculation, the background TOA brightness temperature (BT_b) is defined as the non-burning portion of the pixel (e.g. Dozier 1981), but this value is not currently obtainable using MODIS data for that pixel. Therefore, the MODIS fire detection algorithm approximates the BT_b via a neighborhood search within a square window that progressively widens as necessary around a potential fire pixel until at least 25% of the pixels in the square are valid background pixels (absence of fire) and the number of these valid pixels is at least eight (Giglio et al., 2003; Kaufman et al., 1998a). Not surprisingly, this method may result in a large difference between the in-pixel BT_b and the background temperature estimated by MODIS (hereafter BT_{bm}) especially with large VZAs.

5.1. Mischaracterization of the MODIS 11 μm background temperature

The bi-spectral approach in the MODIS sub-pixel algorithm requires an accurate estimation of both the 4 and 11 μm BT_{bm} (Peterson et al., in press). While the MODIS fire detection algorithm uses the same fire-free pixels to compute the BT_{bm} for the 4 and 11 μm channels (Giglio et al., 2003; Justice et al., 2002), few, if any, subsequent calculations (e.g. FRP_p) require the use of the 11 μm BT_{bm}, thus any errors at 11 μm may have gone unnoticed or have been disregarded. For example, 3 out of the 37 MODIS fire pixels used in the test cases have a pixel brightness temperature that is less than the BT_{bm} at 11 μm, while the 4 μm brightness temperatures display no such mischaracterization (Fig. 6). The three pixels with an error also occur during the daytime, which may increase the background noise due to unequal heating of the surface. Regardless, any such error produces a major limiting factor on the retrieval because sub-pixel calculations are not possible for any of these pixels, unless an improved background characterization technique is developed. Zhukov et al. (2006) described a similar issue with the Bi-Spectral Infrared Detection (BIRD) small satellite mission (operational from 2001 to 2004), but the spectral properties, pixel resolution, and background temperature methodology were significantly different from the MODIS sensor.
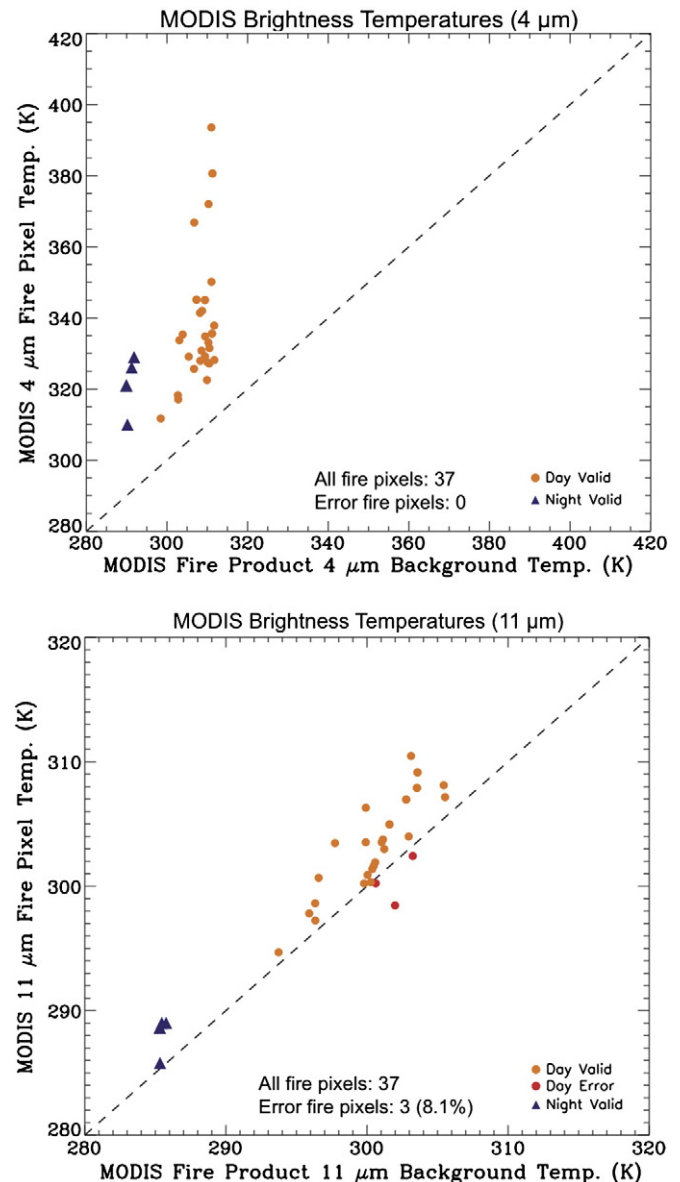
Fig. 6. Scatterplots showing the pixel and background brightness temperatures at 4 μm (top) and 11 μm (bottom) for each MODIS fire pixel from the California test cases. Day and night observations are displayed as dots and triangles, respectively. The color scheme indicates whether each day or night pixel is valid or has a background temperature mischaracterization error. (For interpretation of the references to color in this figure legend, the reader is referred to the web version of this article.)

As described in Section 3, the MODIS 11 μm channel is much more sensitive to the relative change of cooler temperatures than the 4 μm channel, suggesting that the BT_{bm} mischaracterization observed in the three MODIS fire pixels is most likely to occur when the sub-pixel fire area is very small (Zhukov et al., 2006). Therefore, to create a spatial perspective on the sub-pixel fire properties of these pixels, the AMS data are incorporated (Fig. 7a–c) and show that all three fire pixels actually contain fairly large sub-pixel fire area fractions (~0.01). However, two of the pixels (Fig. 7a and b) contain very diffuse fire hot spots and the remaining pixel (Fig. 7c) contains pixel edge hot spots, which can greatly reduce the mean fire pixel temperature due to point spread function effects (Calle et al., 2009; Peterson et al., in press). Furthermore, the 11 μm AMS data (free from saturation) can be averaged to provide a general representation of the sub-pixel fire brightness temperature (FT_{AMS}), which will be considerably lower than at 4 μm due to the reduced sensitivity to higher temperatures, but will still be the warmest portion of the
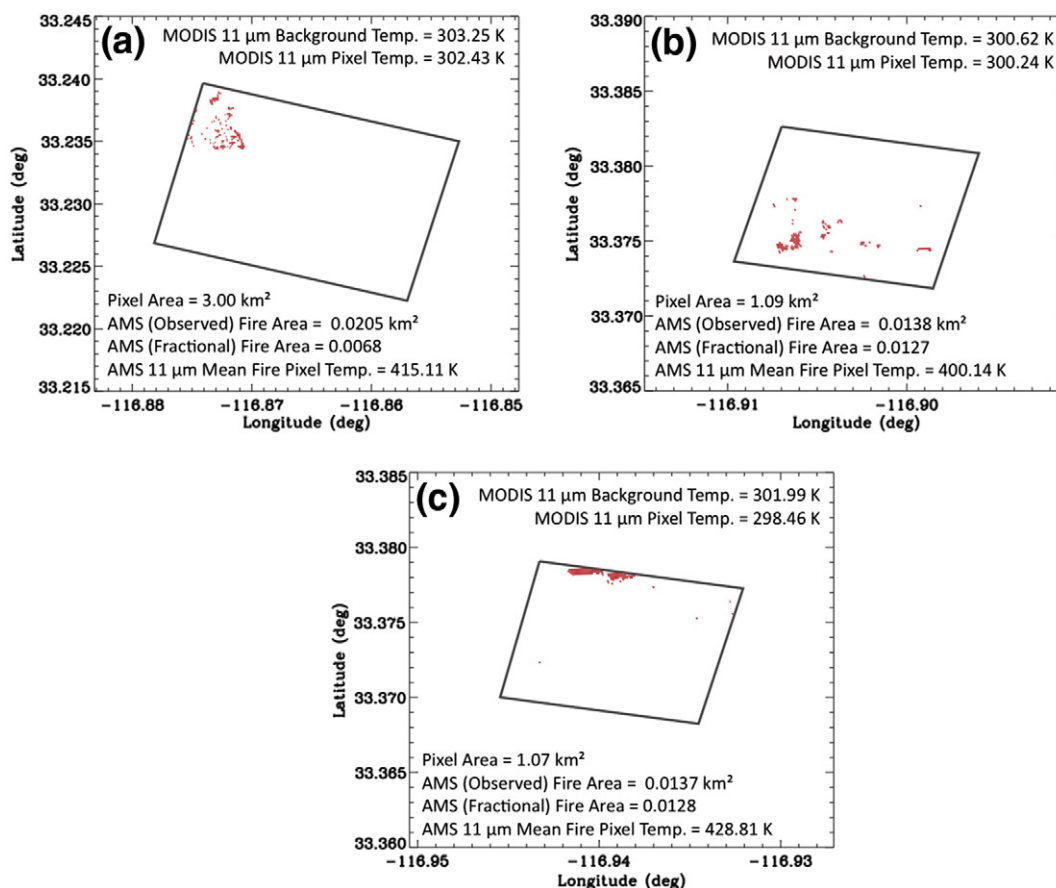
Fig. 7. Spatial displays of the AMS-derived fire locations (red shading) within the three MODIS fire pixels (a–c) that have a brightness temperature less than the background. Black polygons indicate the boundaries of each MODIS fire pixel. (For interpretation of the references to color in this figure legend, the reader is referred to the web version of this article.)

pixel. This analysis shows that the three MODIS fire pixels displayed in Fig. 7a–c have a mean 11 μm FT_{AMS} less than 430 K, which is low in comparison to highly concentrated sub-pixel fire fronts that can produce mean 11 μm FT_{AMS} greater than 460 K (Peterson et al., in press). Therefore, the observed combination of diffuse or pixel edge hot spots, at relatively low FT_{AMS} values, likely reduces the mean MODIS 11 μm fire pixel brightness temperature to the point where it cannot be distinguished from general background noise.

At 11 μm, background noise can result from large burn scars, smoldering regions, or a relatively warm, heterogeneous location (Schroeder et al., 2010). Additional variations in BT_{bm} may result from changes in land cover (e.g. forest to exposed rock), topography, and aspect. The test cases used in this analysis are in fairly mountainous terrain in California (Fig. 1), a situation that may produce variations in BT_{bm} from high to low elevations and from slopes that face the sun (south slopes) versus slopes that face away from the sun (north), as well as vegetated to non-vegetated regions. Fig. 8a and b highlights the 11 μm background noise surrounding the three pixels with an 11 μm mischaracterization using the MODIS and high-resolution AMS data. While there is an offset of about 5 K between sensors (produced from differences in altitude and scan method), both scans (Fig. 8a and b) show how complex topography and changes in aspect produce variations in 11 μm temperature of more than 10 K over very short distances in these daytime scenes. It is also evident that all three non-valid fire pixels (white shading in Fig. 8) are located in a relatively cool region of the scan with much warmer regions in the immediate vicinity. Therefore, depending on how wide the MODIS background pixel window becomes, the resulting mean 11 μm BT_{bm} has the potential to be warmer than the fire pixel temperature, especially since as many as 21 valid (non-fire) background pixels may be included (e.g. Giglio et al., 2003; Kaufman et al., 1998a). With the pixel-level retrieval rendered impossible, these background temperature

errors will affect the FRP_f and effectively reduce the retrieved fire area in the corresponding fire pixel cluster, thus a quality control flag is currently being considered.

5.2. Retrieval uncertainty associated with background temperature

While MODIS is limited to a background window approximation, the AMS data allow the true in-pixel background brightness temperature (BT_{bp}) to be calculated based on the distribution of AMS pixel temperatures at 4 and 11 μm within the MODIS pixel footprint (Peterson et al., in press). Fig. 9a and b shows that the BT_{bp} and BT_{bm} are strongly correlated ($R_{4 μm} = 0.88$ and $R_{11 μm} = 0.92$), but for many pixels, the BT_{bm} is cooler than the BT_{bp}, which may result from differences in sensor characteristics. For the daytime test cases, these deviations are reduced at the smallest VZAs (blue data points), suggesting that off-nadir pixel growth may influence the background temperature noise. However, there is paucity of available data and the test cases with the largest VZAs (64°) occur at night with no solar impact, which may explain the stronger agreement between BT_{bp} and BT_{bm} in the largest VZA cases (orange data points). Even still, Fig. 9a and b shows that there can be a considerable difference between the MODIS fire product and the AMS-derived in-pixel background brightness temperatures.

The incorporation of AMS data also allows the variability (± 1.0 standard deviation) of the BT_{bp} region (e.g. not flaming or smoldering) to be visualized (gray error bars in Fig. 9a,b). From this illustration, it is clear that the 4 μm BT_{bp} region contains a larger range in temperature (~10 K) than at 11 μm (~5 K), suggesting that solar reflectivity may play a role. In general, the variability of the BT_{bp} increases as the VZA (pixel size) increases. However, the MODIS fire pixels at the largest VZAs are nighttime test cases where the temperature variability in the background region of the pixel should be reduced. At 4 μm (and to a
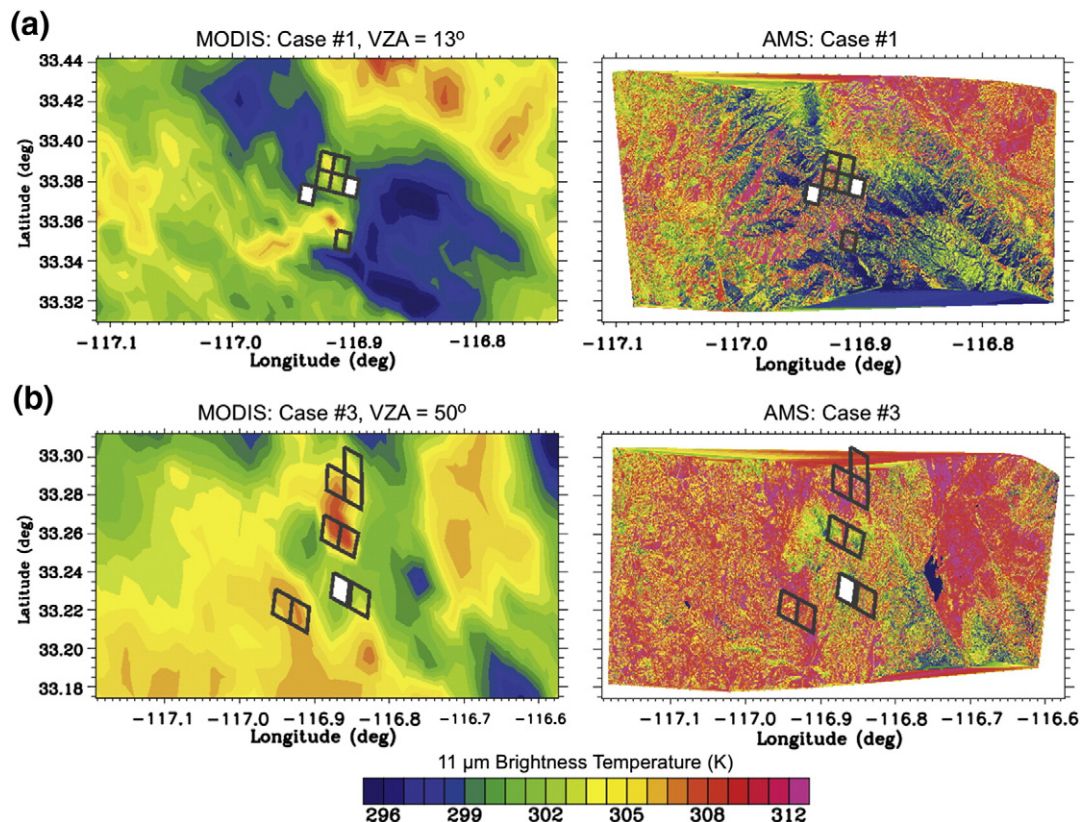
Fig. 8. Maps showing the 11 μm brightness temperature for MODIS (left) and AMS (right) using California test case #1 (a) and case #3 (b). Black polygons indicate the boundaries of MODIS fire pixels and a white-filled polygon indicates a MODIS fire pixel with a brightness temperature that is less than the background.

lesser extent at 11 μm), many of these nighttime, large VZA pixels have the largest variability in the BT_{bp}. In these cases, the large size of the background region may outweigh the effect of nighttime observation by allowing a wider variety of surface features, such as valleys and ridges (complex topography), to be contained within the boundaries of the MODIS fire pixel, greatly affecting the sub-pixel temperature distribution, even at night. Therefore, Fig. 9a and b also highlights the complexities in obtaining an accurate background temperature in a heterogeneous environment, where relatively large variations can occur even within the boundaries of an individual MODIS fire pixel.

The impacts from these background brightness temperature errors on the sub-pixel results are drastically different between the 4 and 11 μm channels. Based on Fig. 9a, it is possible to observe a 4 μm BT_{bp} error of 5 to 10 K. However, an error of 5 K produces a relatively small change in retrieved fire area, averaging 23.0% (Fig. 9c, Table 2). The effect on FRP_f and the cluster FRP_f flux is also small, with mean changes of 13.7% and 20.8%, respectively (Table 2). The error bars in Fig. 9c display the resulting fire area variability on a per pixel basis, produced by running the sub-pixel retrieval with deviations of ± 1.0 K from the observed BT_{bm} up to a maximum deviation of ± 5.0 K. A closer examination reveals that the resulting change in retrieved fire area is very small for large fires with a high FRP_f (~4%) and larger for smaller fires with lower FRP_f values (40–50%). This discrepancy can be explained by fires with a high FRP_f coinciding with a much larger difference between the flaming and the background regions than with low FRP_f fires. Therefore, high FRP_f fires are not as susceptible to BT_{bm} errors as low FRP_f fires.

At 11 μm (Fig. 9d), the error bars were produced by running the sub-pixel retrieval with deviations of ± 0.5 K from the observed BT_{bm} up to a maximum deviation of ± 1.0 K, provided that the BT_{bm} was cooler than the fire pixel brightness temperature. In this case, the small 1.0 K error in 11 μm BT_{bm} produces in an enormous change in retrieved fire area, occasionally reaching an order of magnitude or more. As with

4 μm, smaller fires with low FRP_f are affected more than larger fires with a high FRP_f, but the smallest change in retrieved fire area is still at least 50% (Table 2). The incomplete error bars in Fig. 9d show that this simulation of a small BT_{bm} error still resulted in several pixels that reached the mischaracterization threshold described in the previous section, where the retrieval was rendered impossible because the BT_{bm} became warmer than the pixel brightness temperature. Not surprisingly, the large errors observed in Fig. 9d also produce relatively large deviations in FRP_f, which increase with large VZAs (Fig. 9e). Similarly, the variability in FRP_f, along with the large effect on retrieved fire area, greatly influences the cluster FRP_f flux values, which change by more than 90% for all six fire clusters (Fig. 9f). However, this variability of FRP_f flux (at both 4 and 11 μm) is based solely on the highly sensitive fire area component (denominator in Eq. 7). Therefore, Fig. 9f represents a worst-case scenario for an error of ± 1.0 K, and any variations in FRP_f (shown in Fig. 9e) may mitigate the FRP_f flux sensitivity. Similarly, a cluster that is primarily comprised of fire pixels with high FRP_f values (e.g. >150 MW) will reduce the FRP_f flux sensitivity via the fire area component (Fig. 9d).

6. Discussion

The previous three sections clearly show that several potential direct sources of error in the sub-pixel retrieval (summarized in Table 2), such as the atmospheric profile and background emissivity assumptions, are contained within the uncertainty range of small (± 1.0 K) errors in the 11 μm BT_{bm}. Furthermore, the BT_{bp} displayed in Fig. 9b shows that variations in the 11 μm BT_{bm} may occasionally reach up to 5 K, greatly increasing the uncertainty displayed in Fig. 9d. The sensitivity analysis of Giglio and Kendall (2001) showed a similar results, where the retrieved fire area was roughly 10 times more sensitive to errors in the 11 μm background brightness temperature than at 4 μm. Therefore, this
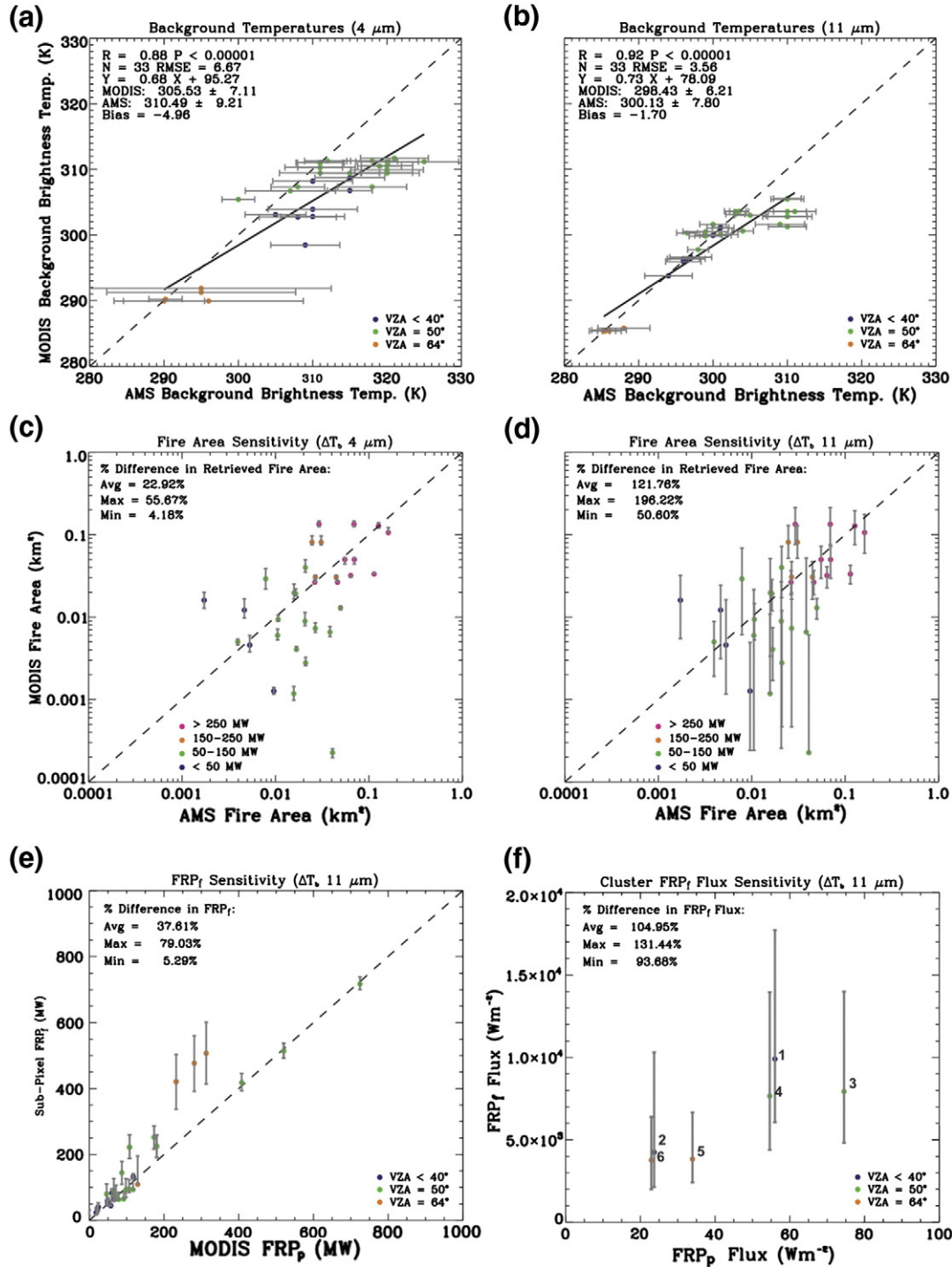
Fig. 9. Retrieval sensitivity to background brightness temperature. (a) and (b) Comparisons between the MODIS fire product BT_{bm} and the AMS derived in-pixel BT_{bp} at 4 and 11 μm, respectively. The color scheme indicates the MODIS viewing zenith angle (distance from nadir). Gray error bars indicate ± 1.0 standard deviation of all AMS data points considered for the calculation of the BT_{bp}. (c) and (d) Pixel-level comparisons between retrieved MODIS fire area and AMS observed fire area from the six California test cases. Gray error bars indicate the sensitivity of the retrieval to a ± 5.0 K error in the 4 μm BT_{bm} and a ± 1.0 K error in the 11 μm BT_{bm}, respectively. The color scheme indicates the FRP_f value for each pixel. (e) Same as (d), but for pixel-level comparisons between MODIS FRP_p and the sub-pixel FRP_f. The color scheme indicates the MODIS viewing zenith angle. (f) Same as (e) and (d), but for cluster-level comparisons between FRP_p per cluster pixel area (FRP_p flux) and FRP_f per fire area (FRP_f flux) using the sum of pixel-level retrievals method. The test case labels correspond to Fig. 1.

analysis confirms the results of previous theoretical studies (e.g. Giglio and Kendall, 2001; Zhukov et al., 2006), and suggests that the 11 μm BT_{bm} is the primary factor limiting the accuracy of sub-pixel calculations, especially for small fires with a low FRP_f.

The results from this study suggest that the atmospheric profile assumption is the second principle source of error (Table 2), and will overestimate retrieved fire area for fire pixels observed in regions of low column water vapor amount, when using the current methodology. However, incorporating multiple profiles into the retrieval process and matching the observed column water vapor amount to the closest atmospheric profile can easily alleviate this problem. Therefore, the BT_{bm} selection methodology is the primary focus for improvement, especially for future satellite missions, such as NPP VIIRS and GOES-R. Currently, BT_{bm} selection is heavily weighted on the 4 μm channel to ensure the

region is free of smoldering or recently burned pixels (Giglio et al., 2003), but a correction for noise caused by variations in surface features is also required, especially at 11 μm. Any future 11 μm background brightness temperature selection methodology will likely require the incorporation of topography, land cover, and aspect data sets. The background region could then be defined as nearby pixels that are not only free of fire, but also have similar characteristics as the fire pixel under scrutiny.

The results in Table 2 show that fire area is typically the most sensitive retrieved parameter to errors in the direct input variables, while FRP$_f$ is much less susceptible due to offsetting effects from fire area fraction and temperature. Peterson et al. (in press) also showed that FRP$_f$, by itself, can be used as an alternative methodology to the current MODIS FRP$_p$, at least for the fire pixels contained within these six California wildfire test cases. However, the primary reason for choosing the sub-pixel based method is that it also allows the radiant energy released over the area of the fire to be quantified via the FRP$_f$ flux (Eq. 7), which may be useful for future fire weather and smoke modeling studies. The FRP$_f$ flux is also the second most sensitive parameter in the retrieval. Therefore, it is desirable to investigate its relationship to key meteorological variables affecting smoke production, such as wind speed, over a broad spatiotemporal domain with known variations in column water vapor amount and background emissivity. Similarly, the total number and spatial distribution of fire pixels with an 11 μm background temperature error (described in Section 5.1) must also be investigated in greater detail. To accomplish these goals, the sub-pixel retrieval was applied to a recent independent case study, explained in the following section.

7. Case study of Texas and Oklahoma wildfires

As an independent test, the MODIS sub-pixel retrieval is applied to a recent, large wildfire event, occurring between 4 September 2011 (00:00 Z) and 8 September 2011 (23:59 Z), where the utility of the FRP$_f$ flux and the spatiotemporal distribution of background temperature errors can easily be explored. The specific study region, located within the United States and Mexico, is bounded by a range of 25–37 north latitude and 93–107 west longitude (Fig. 10), but the primary focus is on the states of Texas and Oklahoma. Several months of persistent upper-level ridging, with 500 hPa heights averaging 5–20 m above the 1981–2010 climatology (contours in Fig. 10), resulted in extreme drought conditions over the majority of the study region. The five days of this case study were also marked by low relative humidity values and stronger than average surface winds, following the passage of a surface cold front. Not surprisingly, 890 MODIS fire pixels were observed (via Aqua and Terra) within the study region during the temporal window of this study (red dots and greed dots in Fig. 10), with the vast majority observed in northeastern Texas and southeastern Oklahoma. This region is an ideal location for testing the sub-pixel retrieval due to the combination of uniform, post-frontal weather conditions and relatively homogeneous biomass and terrain.

7.1. Comparisons to the California test cases

For this application, level-2 MODIS column water vapor data (King et al., 2003) were saved along with the retrieval output for each fire pixel, and show that the average atmospheric column water vapor amount over the five days was 2.09 g/cm^2, which is closer to the mid-latitude summer column water vapor amount of 2.92 g/cm^2 than the California test cases. However a large range of 0.60 to 6.74 g/cm^2 was also observed, due to the study domain stretching from desert regions to the Gulf of Mexico. The majority of the fire pixels are located in northeastern Texas, where the column water vapor amount likely falls much closer to the mean, suggesting that any resulting retrieval errors will be minor, especially compared to the test cases (e.g. Fig. 5). The few fire pixels in the western portion of the study region have column water vapor contents that are much closer to the California test cases (e.g. <1.0 g/cm^2), and thus will suffer from an overestimation in retrieved fire area. However, specific pixel-level validations of retrieved fire area, via AMS (or any other method), were not possible. A detailed examination of the background emissivity was also not considered due to the minimal sensitivity effect shown earlier (Table 2), but the extreme drought likely resulted in regions of brown vegetation that may produce a minor effect on the retrieval output.

The retrieved FRP$_f$ in the study region, like the results from the California test cases (Peterson et al., in press), is strongly correlated (R = 0.97) to the current MODIS FRP$_p$ for the valid individual fire pixels (not shown). However, this case study exposed a secondary limitation of the retrieval, where 39 fire pixels (not considered in the correlation above) had retrieved fire temperatures of 1500 K — the maximum value currently considered in the sub-pixel retrieval based on earlier studies (Giglio and Kendall, 2001; Zhukov et al., 2006). Many of these pixels have an FRP$_f$ that compares nicely to the FRP$_p$, but 11 pixels have an FRP$_f$ that is unrealistically high. One explanation is that retrieval limit of 1500 K may be too low, which is evidenced by the questionable pixels corresponding to large differences between the 11 μm pixel and background temperatures. For example, Zhukov et al. (2006) allowed the retrieved fire temperature to increase above 1500 K if the 11 μm (TIR) pixel brightness temperature was greater than the background temperature plus four standard deviations of the surrounding background noise. However, for this case study, it is generally observed that many of the 1500 K fire temperatures correspond to very low FRP$_p$ values (<140 MW), reduced MODIS confidence levels, and small retrieved fire area fractions (<0.001). Therefore, these are likely small fires, such as a fire front in a grassland or pasture (e.g. Mell et al., 2007; Smith et al., 2005; Stephens et al., 2008), which are also situations that greatly increase the uncertainty in the retrieval output (e.g. Giglio and Kendall, 2001; Peterson et al., in press). As a result, the retrieved fire temperature of 1500 K may simply be an artifact of an underestimated 11 μm background temperature that produces an improper fit (artificially large difference between fire and background) in the observed radiances during the retrieval process (Peterson et al., in press).

The 11 μm BT$_{bm}$ mischaracterization errors, highlighted in the California test cases (background warmer than the fire pixel), are also present in this case study, denoted by the green dots in Fig. 10. Specifically, 157 (17.6%) of the 890 MODIS fire pixels have this BT$_{bm}$ error, but seem to be randomly distributed within the study region, suggesting there is little spatial dependence on background noise. The vast majority of these errors, including the largest magnitudes, occur with daytime pixels (Fig. 11 and Table 3), where 26.4% of the pixels have an error. The case study domain has minimal topographic influences compared to the California test cases, suggesting that the 11 μm BT$_{bm}$ errors in
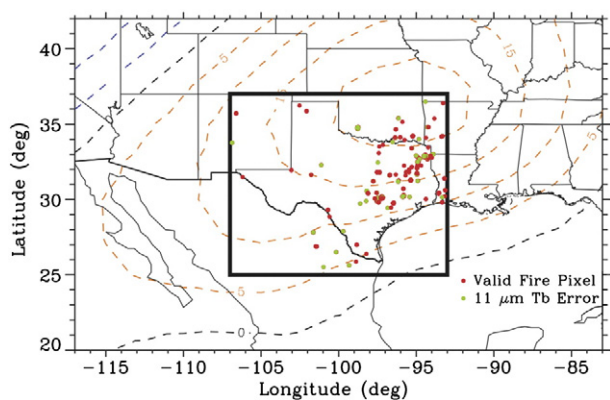
Fig. 10. Map of the case study region, as denoted by the black box. The MODIS fire pixels observed between 4 and 8 September 2011 are displayed as dots, with red indicating valid pixels and green indicating an error in the 11 μm background temperature. Dashed contours indicate the mean 500 hPa height anomalies (based the 1981–2010 climatology) during the preceding three months (June, July, and August), with red and blue respectively indicating positive and negative anomalies.

eastern Texas and Oklahoma likely stem from variations in local land cover (http://gisdata.usgs.gov/website/mrlc/viewer.htm), which may include forest (deciduous/evergreen), cropland, pasture land, and urban or other non-vegetated regions. The major drought may also have created localized cases of brown or de-vegetated regions (presumably not irrigated) that are located nearby green, irrigated regions, which will have a considerably lower 11 μm BT_{bm} than the dry regions. Therefore, similar to the California test cases, daytime background noise at 11 μm is the key factor limiting the sub-pixel retrieval in this case study, further supporting the need for an improved BT_{bm} selection methodology. In stark contrast, the 4 μm background brightness temperatures displayed in Fig. 11 are clearly free of any mischaracterization errors due to the channel's reduced sensitivity to cooler temperatures.

7.2. Example application of FRP_f flux: fire weather

When considering the very nature of fire events, FRP is an excellent parameter to focus on because it is a direct measurement of fire intensity (Ichoku et al., 2008a). However, since the advent of satellite-derived FRP products, few, if any, studies have investigated the relationship between FRP and meteorological variables. Peterson et al. (2010) did attempt to investigate any such relationships (via MODIS FRP_p) over broad spatial domains located within the boreal forest of North America, but showed that there is a very weak correlation between FRP_p and most fire-related weather variables, except for the overall synoptic environment (e.g. 500 hPa heights). The lack of any significant correlation between FRP_p and the meteorological variables (e.g. wind speed), which are assumed to greatly influence its intensity, likely stems from the lack of fire size information in the current MODIS FRP_p data. Therefore, improved results are expected when using FRP_f flux, especially for large, intense fire events.

For this case study, meteorological data were obtained from the North American Regional Reanalysis (NARR), which blends a variety of observational data into Eta model output containing 45 vertical layers across the North American continent with ~32 km grid spacing every three hours (Ebisuzaki, 2004; Mesinger et al., 2006). The NARR data were subsequently downscaled onto a 10 km grid with one-hour temporal resolution by the Weather Research and Forecasting (WRF) model (e.g. Grell et al., 2005; Skamarock et al., 2005; Wang et al., in press), and the MODIS fire observations, including the sub-pixel output, were geographically matched to the mesh of 10 km grid boxes and summed for each day. This data integration step is essentially the same as the clustering sum of pixel-level retrievals methodology (described in Section 2.2, Peterson et al., in press), and acts to reduce the effects from several potential sources of error (e.g. PSF effects). Therefore, the grid boxes with a higher number of MODIS fire pixels will likely provide retrieved fire area with a higher accuracy. However, the previously described sensitivity to direct sources of error (e.g. improper BT_{bm} selection) may still be present, especially when the average FRP_f is low.

While the California test cases allowed for a simple creation of fire clusters, composed of several, mostly contiguous MODIS fire pixels, the case study domain described here (Fig. 10) includes many fire pixels that may not be part of a contiguous cluster. In addition, the relatively large MODIS pixel size, varying from 1 to 10 km (depending on VZA), also limits the number of observed contiguous pixels. Therefore, investigating FRP_f flux for all fire pixels contained within a 10 km grid box (or any similar model grid) is the most advantageous application of a clustering methodology for MODIS data. Additional output includes the number of fire pixels, total fire area, total FRP_f, and the total FRP_p for each grid box, as well as the total number of invalid pixels, currently produced from 11 μm BT_{bm} errors and reaching the fire temperature threshold of 1500 K. These fire data can then be compared to the meteorological data from each model grid box at each one-hour time step.

Drawing from the widely used Canadian Forest Fire Danger Rating System (CFFDRS), surface wind speed and temperature are key variables affecting fire-spread potential (Van Wagner, 1987; Van Wagner and
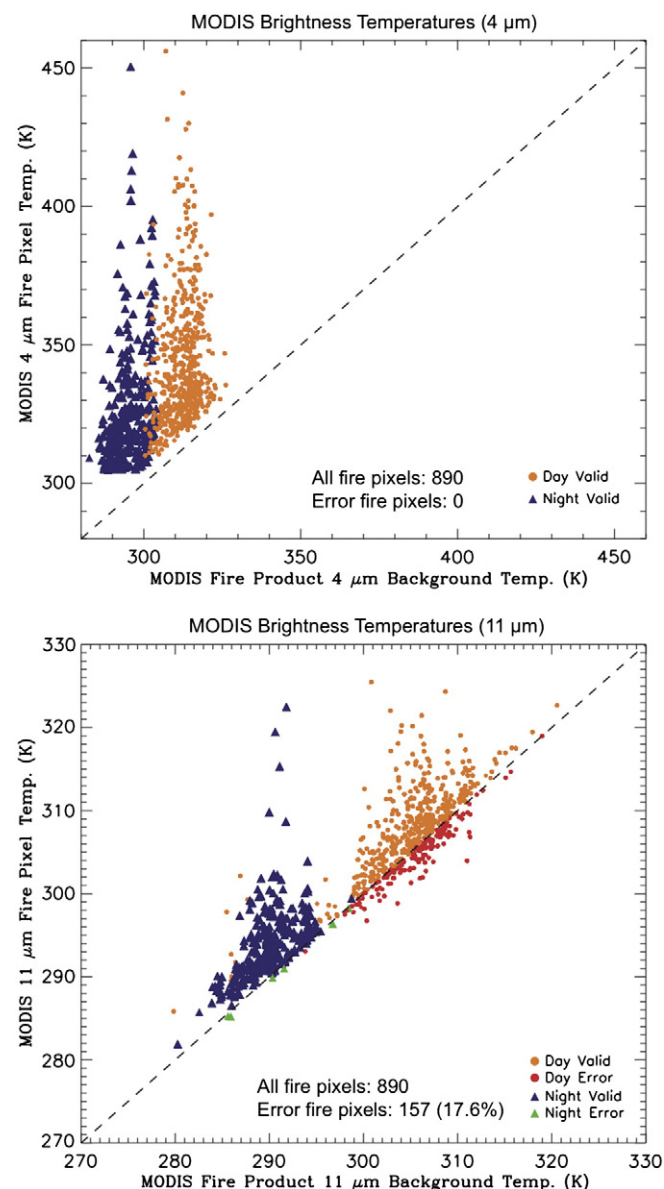

Fig. 11. Scatterplots showing the pixel and background brightness temperatures at 4 μm (top) and 11 μm (bottom) for each MODIS fire pixel from the case study application. Day and night observations are respectively displayed as dots and triangles. The color scheme indicates whether each day or night pixel is valid or has a background temperature error. The corresponding statistical summary is provided in Table 3. (For interpretation of the references to color in this figure legend, the reader is referred to the online version of this chapter.)

Pickett, 1985), and should therefore be strongly correlated to the FRP observations. However, Fig. 12a and c shows there is very little correlation between MODIS FRP_p and the surface (10-meter) wind speed or temperature ($R_{wind} = 0.14$ and $R_{temp} = 0.18$). When using the FRP_f flux

Table 3
Statistics for the MODIS 11 μm background brightness temperature.

Observation	Number of pixels	Pixels with error	% error
California test cases (development)			
All pixels	37	3	8.1
Day pixels	32	3	9.4
Night pixels	5	0	0.0
Case study (application)			
All pixels	890	157	17.6
Day pixels	571	151	26.4
Night pixels	319	6	1.90
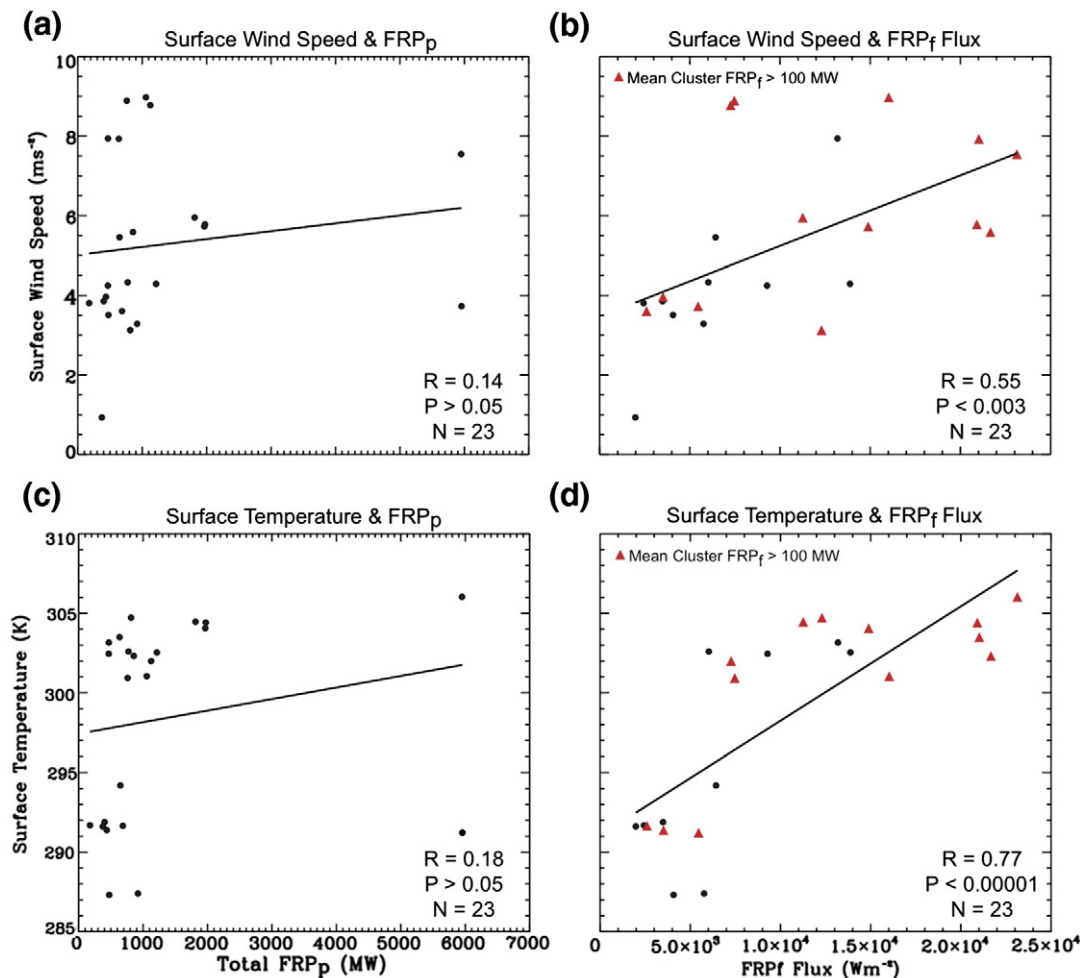
Fig. 12. Analysis of meteorological and satellite-retrieved parameters for the 23 largest fire clusters in the case study domain (displayed in Fig. 10). (a) Relationship between the MODIS FRP_p and surface (10-meter) wind speed. (b) Relationship between the cluster FRP_f flux and surface wind speed. (c) and (d) Same and (a) and (b) but for the surface (10-meter) temperature. The solid black line corresponds to the linear fit equation. R, P, and N denote the linear correlation coefficient, P-value, and number of data points, respectively. Red triangles in (b) and (d) indicate a fire pixel cluster with a mean $FRP_f > 100$ MW. (For interpretation of the references to color in this figure legend, the reader is referred to the web version of this article.)

(Fig. 12b and d), the correlations with surface wind speed and temperature are significantly stronger ($R_{wind} = 0.55$ and $R_{temp} = 0.77$). In addition, the mean FRP_f for 13 (57%) of these fire pixel clusters is greater than 100 MW (red triangles in Fig. 12), suggesting that the large sensitivity to BT_{bm} errors will be reduced via the fire area component (e.g. Fig. 9d). While these results are very encouraging, it is important to note that Fig. 12 only shows the 23 largest fire clusters, defined as a WRF grid box with at least six valid fire pixels.

The effect of variations in cluster size threshold is examined in Fig. 13 by computing the correlation between the FRP and meteorological data for several fire pixel cluster size thresholds, ranging from 1 to 12 (a threshold of 12 indicates a cluster size ≥ 12 fire pixels). As random effects are averaged out, the correlations using FRP_f flux increase rapidly, become statistically significant, and begin to stabilize at a threshold of ~6 pixels, which is used in Fig. 12. In contrast, the correlations using the MODIS FRP_p remain very low ($R < 0.20$), and are not statistically significant for nearly every cluster size. This suggests that FRP_f flux may be an improvement over FRP_p for characterizing fire weather, especially for large fire pixel clusters. However, as described earlier, this case study is an idealized fire event with generally uniform meteorological conditions within a region that is devoid of any major topography. Therefore, attempting to identify relationships between meteorological variables and FRP_f flux in regions with complex topographic features, and potentially large mesoscale variability, will be more challenging.
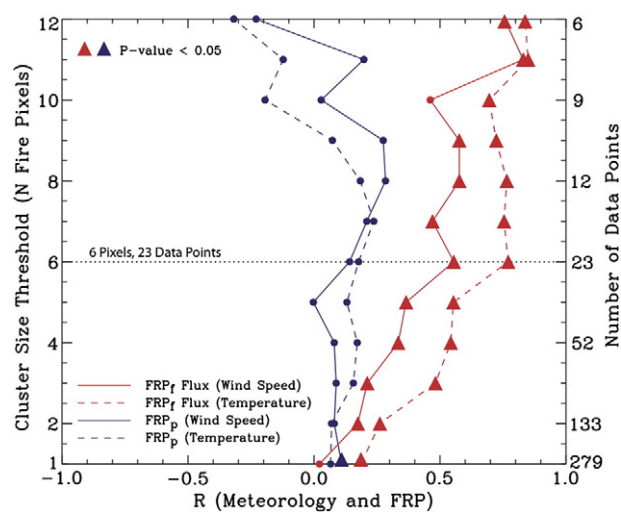
Fig. 13. Correlations between the FRP data and the meteorological variables of surface wind speed (solid) and temperature (dashed) as a function of fire pixel cluster size and the number of available data points. Red curves indicate FRP_f flux and blue curves indicate FRP_p. Triangles are used to identify statistical significance, corresponding to a P-value < 0.05. The horizontal, dotted line indicates the fire pixel threshold used in Fig. 12. (For interpretation of the references to color in this figure legend, the reader is referred to the web version of this article.)

While this case study used a 10 km model grid, the methodology can easily be applied to any mesoscale model grid mesh. Increasing the grid size will produce larger fire clusters and reduce the uncertainty associated with the fire area component of the FRP_f flux, especially when the mean FRP_f is high. However, larger grid spacing may concurrently decrease the accuracy of the corresponding meteorological information, especially for variables like surface wind speed that often vary over short distances. As a result, caution must be used when integrating meteorological data archives and the MODIS sub-pixel fire output. Future sensors, such as NPP VIIRS (e.g. Csiszar et al., 2011), will have a higher spatial resolution (~750 m), and may allow for clustering based solely on contiguous fire pixel clusters, similar to the BIRD satellite (Zhukov et al., 2006). In these cases, the accuracy of FRP-based fire weather analysis will improve because large fire clusters will be predefined and easily separated from small fires.

8. Summary and conclusions

This study has provided a theoretical sensitivity analysis for the three major outputs of a MODIS sub-pixel retrieval algorithm (fire area, FRP_f, and FRP_f flux) based on direct input variables and assumptions, as well as a case study application. The primary focus is on variations in the atmospheric profile, background emissivity, and background brightness temperature, which were analyzed to varying levels of detail. Results indicate that significant reductions in the retrieved pixel-level fire area will occur if the observed column water vapor is very low with respect to the mid-latitude summer, climatologically based profile. The effect on FRP_f is much smaller because the decrease in retrieved fire area is offset by an increase in retrieved fire temperature. Therefore, the overall sensitivity of the cluster FRP_f flux falls between that of retrieved fire area and FRP_f, but is highly influenced by changes in fire area. In contrast, potential variations in the assumed values for the 4 and 11 μm background emissivities have a minor effect on all retrieval output (e.g. <15% change in fire area and FRP_f), except when fire events are surrounded by large regions of highly reflective, brown vegetation.

When considering all potential sources of direct error, small deviations in the 11 μm BT_{bm} (background noise) have the greatest affect on all retrieval outputs. For example, a ± 1 K error can produce a change in retrieved fire area of more than an order of magnitude, with the potential for large impacts on FRP_f and the cluster FRP_f flux as well. For some MODIS fire pixels, the sub-pixel retrieval can even become irrelevant when the 11 μm BT_{bm} (provided by MODIS) is greater than the pixel brightness temperature. The case study application showed that 17.6% of the 890 available fire pixels suffered from this BT_{bm} error, with the vast majority, especially the large magnitude errors, occurring in daytime scenes. With this limitation, any future applications will require an improved background brightness temperature selection methodology, based on land cover, topographic, and aspect data sets. In fact, the impacts of any potential land cover variations or vegetation health on background temperature noise can easily be explored using additional satellite data sets (e.g. NDVI).

The results of this study suggest that the large sensitivity of the sub-pixel retrieval output can be reduced when investigating large fire clusters (at least 6 MODIS fire pixels). This is especially true when the cluster is comprised of fire pixels with a high FRP_f (e.g. >150 MW), which reduces the sensitivity to BT_{bm} errors by producing a larger difference between the flaming and the background regions. As shown in the case study, fire pixel clusters can be defined based on the resolution of a mesoscale model grid. Subsequent comparisons with meteorological data showed that the cluster FRP_f flux, unlike the current MODIS FRP_p, has a statistically significant correlation with surface wind speed and temperature, especially for large fire clusters. This encouraging result suggests that the cluster FRP_f flux may be useful for characterizing the meteorological effects on fire intensity. However, future studies are warranted to further investigate the utility of FRP_f flux in fire weather analysis using a variety of spatiotemporal domains with variations in model grid spacing.

Perhaps the most desirable application of FRP_f flux is improving smoke emission estimates and transport forecasts. While earlier studies (e.g. Val Martin et al., 2010) suggest that regions of high FRP_p commonly result in higher altitude smoke plumes, the FRP_f flux provides an estimation of the rate of energy release over the fire area itself, and is therefore directly related to the thermal buoyancy of the smoke plume (Kahn et al., 2007; Lavoue et al., 2000). However, the large sensitivity of FRP_f flux, especially due to BT_{bm} errors, will likely constrain any future smoke injection height analysis to the largest and most intense fire events. Improved plume height estimates have the most value for these large fire events due to the increased chance of injection above the boundary layer. Therefore, despite the limitations, FRP_f flux may prove useful for identifying the cases where smoke is most likely to be injected into the free troposphere and transported a great distance, especially when using the higher-resolution sensors (e.g. NPP VIIRS) that will replace MODIS over the next decade (Csiszar et al., 2011).

Acknowledgments

References

Ambrosia, V. G., Sullivan, D. V., & Buechel, S. W. (2011a). Integrating sensor data and geospatial tools to enhance real-time disaster management capabilities: Wildfire observations. *Societal Challenges and Geoinformatics, 482*, 1–12.

Ambrosia, V. G., & Wegener, S. (2009). Unmanned airborne platforms for disaster remote sensing support. In Pei-Gee Peter Ho (Ed.), *Geoscience and remote sensing* (pp. 91–114). (InTech).

Ambrosia, V. G., Wegener, S., Zajkowski, T., Sullivan, D. V., Buechel, S., Enomoto, F., et al. (2011b). The Ikhana unmanned airborne system (UAS) western states fire imaging missions: From concept to reality (2006–2010). *Geocarto International, 26*, 85–101.

Cahoon, D. R., Jr., Stocks, B. J., Levine, J. S., Cofer, W. R., III, & Chung, C. C. (1992). Evaluation of a technique for satellite-derived area estimation of forest fires. *Journal of Geophysical Research, 97*, 805–3814.

Calle, A., Casanova, J. L., & Gonzalez-Alonso, F. (2009). Impact of point spread function of MSG-SEVIRI on active fire detection. *International Journal of Remote Sensing, 30*, 4567–4579.

Csiszar, I. A., Schroeder, W., Giglio, L., Justice, C. O., & Ellicott, E. (2011). Quantitative evaluation of active fire detection capabilities from VIIRS. *91st American Meteorological Society annual meeting. Seattle, WA.*

Damoah, R., Spichtinger, N., Servranckx, R., Fromm, M., Eloranta, E. W., Razenkov, I. A., et al. (2006). A case study of pyro-convection using transport model and remote sensing data. *Atmospheric Chemistry and Physics, 6*, 173–185.

Dennison, P. E., Charoensiri, K., Roberts, D. A., Peterson, S. H., & Green, R. O. (2006). Wildfire temperature and land cover modeling using hyperspectral data. *Remote Sensing of Environment, 100*, 212–222.

Dozier, J. (1981). A method for satellite identification of surface temperature fields of subpixel resolution. *Remote Sensing of Environment, 11*, 221–229.

Duck, T. J., Firanski, B. J., Millet, D. B., Goldstein, A. H., Allan, J., Holzinger, R., et al. (2007). Transport of forest fire emissions from Alaska and the Yukon Territory to Nova Scotia during summer 2004. *Journal of Geophysical Research-Atmospheres, 112*.

Ebisuzaki, W. (2004). In G. Rutledge (Ed.), *National Climatic Data Center data documentation for NOAA Operational Model Archive and Distribution System (NOMADS) North American Regional Reanalysis* (pp. 1–11). Camp Springs, MD: National Climatic Data Center.

Eckmann, T. C., Roberts, D. A., & Still, C. J. (2008). Using multiple endmember spectral mixture analysis to retrieve subpixel fire properties from MODIS. *Remote Sensing of Environment, 112*, 3773–3783.

Eckmann, T. C., Roberts, D. A., & Still, C. J. (2009). Estimating subpixel fire sizes and temperatures from ASTER using multiple endmember spectral mixture analysis. *International Journal of Remote Sensing, 30*, 5851–5864.

Eckmann, T. C., Still, C. J., Roberts, D. A., & Michaelsen, J. C. (2010). Variations in subpixel fire properties with season and land cover in southern Africa. *Earth Interactions, 14*.

Flannigan, M. D., & Vonder Haar, T. H. (1986). Forest fire monitoring using NOAA satellite AVHRR. *Canadian Journal of Forest Research, 16*, 975–982.

Flasse, S. P., & Ceccato, P. S. (1996). A contextual algorithm for AVHRR fire detection. *International Journal of Remote Sensing, 17*, 419–424.

Gao, B. C., Xiong, X. X., Li, R. R., & Wang, D. Y. (2007). Evaluation of the Moderate Resolution Imaging Spectrometer special 3.95-mu m fire channel and implications on fire channel selections for future satellite instruments. *Journal of Applied Remote Sensing, 1*.

Giglio, L. (2010). MODIS collection 5 active fire product user's guide version 2.4. University of Maryland, Department of Geography.

Giglio, L., Descloitres, J., Justice, C. O., & Kaufman, Y. J. (2003). An enhanced contextual fire detection algorithm for MODIS. *Remote Sensing of Environment, 87*, 273–282.

Giglio, L., & Justice, C. O. (2003). Effect of wavelength selection on characterization of fire size and temperature. *International Journal of Remote Sensing, 24*, 3515–3520.

Giglio, L., & Kendall, J. D. (2001). Application of the Dozier retrieval to wildfire characterization — A sensitivity analysis. *Remote Sensing of Environment, 77*, 34–49.

Giglio, L., Kendall, J. D., & Justice, C. O. (1999). Evaluation of global fire detection algorithms using simulated AVHRR infrared data. *International Journal of Remote Sensing, 20*, 1947–1985.

Grell, G. A., Peckham, S. E., Schmitz, R., McKeen, S. A., Frost, G., Skamarock, W. C., et al. (2005). Fully coupled "online" chemistry within the WRF model. *Atmospheric Environment, 39*, 6957–6975.

Ichoku, C., Giglio, L., Wooster, M. J., & Remer, L. A. (2008a). Global characterization of biomass-burning patterns using satellite measurements of fire radiative energy. *Remote Sensing of Environment, 112*, 2950–2962.

Ichoku, C., & Kaufman, Y. J. (2005). A method to derive smoke emission rates from MODIS fire radiative energy measurements. *IEEE Transactions on Geoscience and Remote Sensing, 43*, 2636–2649.

Ichoku, C., Martins, J. V., Kaufman, Y. J., Wooster, M. J., Freeborn, P. H., Hao, W. M., et al. (2008b). Laboratory investigation of fire radiative energy and smoke aerosol emissions. *Journal of Geophysical Research—Atmospheres, 113*.

Jordan, N. S., Ichoku, C., & Hoff, R. M. (2008). Estimating smoke emissions over the US Southern Great Plains using MODIS fire radiative power and aerosol observations. *Atmospheric Environment, 42*, 2007–2022.

Justice, C. O., Giglio, L., Korontzi, S., Owens, J., Morisette, J. T., Roy, D., et al. (2002). The MODIS fire products. *Remote Sensing of Environment, 83*, 244–262.

Kahn, R. A., Li, W. H., Moroney, C., Diner, D. J., Martonchik, J. V., & Fishbein, E. (2007). Aerosol source plume physical characteristics from space-based multiangle imaging. *Journal of Geophysical Research—Atmospheres, 112*, 20.

Kaiser, J. W., Suttie, M., Flemming, J., Morcrette, J. J., Boucher, O., & Schultz, M. G. (2009). Global real-time fire emission estimates based on space-borne fire radiative power observations. In T. Nakajima, & M. A. Yamasoe (Eds.), *Current problems in atmospheric radiation (IRS 2008) CP1100* (pp. 1–4). American Institute of Physics.

Kaufman, Y. J., Ichoku, C., Giglio, L., Korontzi, S., Chu, D. A., Hao, W. M., et al. (2003). Fire and smoke observed from the Earth Observing System MODIS instrument — Products, validation, and operational use. *International Journal of Remote Sensing, 24*, 1765–1781.

Kaufman, Y. J., Justice, C. O., Flynn, L. P., Kendall, J. D., Prins, E. M., Giglio, L., et al. (1998a). Potential global fire monitoring from EOS-MODIS. *Journal of Geophysical Research—Atmospheres, 103*, 32215–32238.

Kaufman, Y. J., Kleidman, R. G., & King, M. D. (1998b). SCAR-B fires in the tropics: Properties and remote sensing from EOS-MODIS. *Journal of Geophysical Research—Atmospheres, 103*, 31955–31968.

Kelha, V., Rauste, Y., Hame, T., Sephton, T., Buongiorno, A., Frauenberger, O., et al. (2003). Combining AVHRR and ATSR satellite sensor data for operational boreal forest fire detection. *International Journal of Remote Sensing, 24*, 1691–1708.

King, M. D., Menzel, W. P., Kaufman, Y. J., Tanre, D., Gao, B. C., Platnick, S., et al. (2003). Cloud and aerosol properties, precipitable water, and profiles of temperature and water vapor from MODIS. *IEEE Transactions on Geoscience and Remote Sensing, 41*, 442–458.

Kopacz, M., Mauzerall, D. L., Wang, J., Leibensperger, E. M., Henze, D. K., & Singh, K. (2011). Origin and radiative forcing of black carbon transported to the Himalayas and Tibetan Plateau. *Atmospheric Chemistry and Physics, 11*, 2837–2852.

Koren, I., Remer, L. A., & Longo, K. (2007). Reversal of trend of biomass burning in the Amazon. *Geophysical Research Letters, 34*.

Langaas, S. (1993). A parameterized bispectral model for savanna fire detection using AVHRR night images. *International Journal of Remote Sensing, 14*, 2245–2262.

Lavoue, D., Liousse, C., Cachier, H., Stocks, B. J., & Goldammer, J. G. (2000). Modeling of carbonaceous particles emitted by boreal and temperate wildfires at northern latitudes. *Journal of Geophysical Research—Atmospheres, 105*, 26871–26890.

Li, Z., Nadon, S., & Cihlar, J. (2000a). Satellite-based detection of Canadian boreal forest fires: development and application of the algorithm. *International Journal of Remote Sensing, 21*, 3057–3069.

Li, Z., Nadon, S., Cihlar, J., & Stocks, B. (2000b). Satellite-based mapping of Canadian boreal forest fires: evaluation and comparison of algorithms. *International Journal of Remote Sensing, 21*, 3071–3082.

Matson, M., & Dozier, J. (1981). Identification of subresolution high temperature sources using a thermal IR sensor. *Photogrammetric Engineering and Remote Sensing, 47*, 1311–1318.

McClatchey, R. A., Fenn, R. W., Selby, J. E. A., Volz, F. E., & Garing, J. S. (1972). Optical properties of the atmosphere. *AFCRL Environ. Res. Papers No. 411* (pp. 1–108). (Third edition). Bedford. MA: L. G. Hanscom Field.

Mell, W., Jenkins, M. A., Gould, J., & Cheney, P. (2007). A physics-based approach to modelling grassland fires. *International Journal of Wildland Fire, 16*, 1–22.

Mesinger, F., DiMego, G., Kalnay, E., Mitchell, K., Shafran, P. C., Ebisuzaki, W., et al. (2006). North American Regional Reanalysis. *Bulletin of the American Meteorological Society, 87*, 343–360.

Peterson, D., Wang, J., Ichoku, C., Hyer, E., & Ambrosia, V. (in press). A sub-pixel-based calculation of fire radiative power from MODIS observations: 1. Algorithm development and initial assessment. Remote Sensing of Environment.

Peterson, D., Wang, J., Ichoku, C., & Remer, L. A. (2010). Effects of lightning and other meteorological factors on fire activity in the North American boreal forest: implications for fire weather forecasting. *Atmospheric Chemistry and Physics, 10*, 6873–6888.

Petitcolin, F., & Vermote, E. (2002). Land surface reflectance, emissivity and temperature from MODIS middle and thermal infrared data. *Remote Sensing of Environment, 83*, 112–134.

Prins, E. M., & Menzel, W. P. (1992). Geostationary satellite detection of biomass burning in South-America. *International Journal of Remote Sensing, 13*, 2783–2799.

Prins, E. M., & Menzel, W. P. (1994). Trends in South American biomass burning detected with the GOES visible infrared spin scan radiometer atmospheric sounder from 1983 to 1991. *Journal of Geophysical Research—Atmospheres, 99*, 16719–16735.

Randerson, J. T., Liu, H., Flanner, M. G., Chambers, S. D., Jin, Y., Hess, P. G., et al. (2006). The impact of boreal forest fire on climate warming. *Science, 314*, 1130–1132.

Ricchiazzi, P., Yang, S. R., Gautier, C., & Sowle, D. (1998). SBDART: A research and teaching software tool for plane-parallel radiative transfer in the Earth's atmosphere. *Bulletin of the American Meteorological Society, 79*, 2101–2114.

Roberts, G., Wooster, M. J., & Lagoudakis, E. (2009). Annual and diurnal african biomass burning temporal dynamics. *Biogeosciences, 6*, 849–866.

Roberts, G., Wooster, M. J., Perry, G. L. W., Drake, N., Rebelo, L. M., & Dipotso, F. (2005). Retrieval of biomass combustion rates and totals from fire radiative power observations: Application to southern Africa using geostationary SEVIRI imagery. *Journal of Geophysical Research—Atmospheres, 110*.

Roy, D. P., Boschetti, L., Justice, C. O., & Ju, J. (2008). The collection 5 MODIS burned area product — Global evaluation by comparison with the MODIS active fire product. *Remote Sensing of Environment, 112*, 3690–3707.

Sapkota, A., Symons, J. M., Kleissl, J., Wang, L., Parlange, M. B., Ondov, J., et al. (2005). Impact of the 2002 Canadian forest fires on particulate matter air quality in Baltimore City. *Environmental Science and Technology, 39*, 24–32.

Schroeder, W., Csiszar, I., Giglio, L., & Schmidt, C. C. (2010). On the use of fire radiative power, area, and temperature estimates to characterize biomass burning via moderate to coarse spatial resolution remote sensing data in the Brazilian Amazon. *Journal of Geophysical Research, 115*, D21121.

Shephard, M. W., & Kennelly, E. J. (2003). Effect of band-to-band coregistration on fire property retrievals. *IEEE Transactions on Geoscience and Remote Sensing, 41*, 2648–2661.

Skamarock, W. C., Klemp, J. B., Dudhia, J., Gill, D. O., Barker, D. M., Wang, W., et al. (2005). A description of the advanced research WRF version 2. *NCAR Technical Note. Mesoscale and Microscale Meteorology Division, National Center for Atmospheric Research, Boulder, Colorado, USA*.

Smith, A. M. S., Wooster, M. J., Drake, N. A., Dipotso, F. M., & Perry, G. L. W. (2005). Fire in African savanna: Testing the impact of incomplete combustion on pyrogenic emissions estimates. *Ecological Applications, 15*, 1074–1082.

Spracklen, D. V., Logan, J. A., Mickley, L. J., Park, R. J., Yevich, R., Westerling, A. L., et al. (2007). Wildfires drive interannual variability of organic carbon aerosol in the western US in summer. *Geophysical Research Letters, 34*.

Stephens, S. L., Weise, D. R., Fry, D. L., Keiffer, R. J., Dawson, J., Koo, E., et al. (2008). Measuring the rate of spread of chaparral prescribed fires in northern California. *Fire Ecology, 4*, 74–86.

Tang, B. H., Li, Z. L., & Bi, Y. (2009). Estimation of land surface directional emissivity in mid-infrared channel around 4.0 μm from MODIS data. *Optics Express, 17*, 3173–3182.

Val Martin, M., Logan, J. A., Kahn, R. A., Leung, F. Y., Nelson, D. L., & Diner, D. J. (2010). Smoke injection heights from fires in North America: analysis of 5 years of satellite observations. *Atmospheric Chemistry and Physics, 10*, 1491–1510.

van der Werf, G. R., Randerson, J. T., Giglio, L., Gobron, N., & Dolman, A. J. (2008). Climate controls on the variability of fires in the tropics and subtropics. *Global Biogeochemical Cycles, 22*.

Van Wagner, C. E. (1987). Development and structure of the Canadian Forest Fire Weather Index System. Canadian Forestry Service.

Van Wagner, C. E., & Pickett, T. L. (1985). Equations and FORTRAN program for the Canadian forest fire weather index system. *Forestry Technical Report, 33*, Ottawa: Canadian Forestry Service, Government of Canada.

Wang, J., Christopher, S. A., Nair, U. S., Reid, J. S., Prins, E. M., Szykman, J., et al. (2006). Mesoscale modeling of Central American smoke transport to the United States: 1. "Top-down" assessment of emission strength and diurnal variation impacts. *Journal of Geophysical Research—Atmospheres, 111*.

Wang, J., Ge, C., Yang, Z., Hyer, E. J., Reid, J. S., Chew, B. N., Mahmud, M., Zhang, Y., & Zhang, M. (in press). Mesoscale modeling of smoke transport over the Southeast Asian Maritime Continent: interplay of sea breeze, trade wind, typhoon, and topography. Atmospheric Research 7SEAS special issue.

Westphal, D. L., & Toon, O. B. (1991). Simulations of microphysical, radiative, and dynamic processes in a continental-scale forest-fire smoke plume. *Journal of Geophysical Research—Atmospheres, 96*, 22379–22400.

Wolfe, R. E., Nishihama, M., Fleig, A. J., Kuyper, J. A., Roy, D. P., Storey, J. C., et al. (2002). Achieving sub-pixel geolocation accuracy in support of MODIS land science. *Remote Sensing of Environment, 83*, 31–49.

Wooster, M. J. (2002). Small-scale experimental testing of fire radiative energy for quantifying mass combusted in natural vegetation fires. *Geophysical Research Letters, 29*.

Wooster, M. J., Roberts, G., Perry, G. L. W., & Kaufman, Y. J. (2005). Retrieval of biomass combustion rates and totals from fire radiative power observations: FRP derivation and

calibration relationships between biomass consumption and fire radiative energy release. *Journal of Geophysical Research—Atmospheres, 110*.

Wooster, M. J., Zhukov, B., & Oertel, D. (2003). Fire radiative energy for quantitative study of biomass burning: Derivation from the BIRD experimental satellite and comparison to MODIS fire products. *Remote Sensing of Environment, 86*, 83–107.

Zhukov, B., Briess, K., Lorenz, E., Oertel, D., & Skrbek, W. (2005). Detection and analysis of high-temperature events in the BIRD mission. *Acta Astronautica, 56*, 65–71.

Zhukov, B., Lorenz, E., Oertel, D., Wooster, M., & Roberts, G. (2006). Spaceborne detection and characterization of fires during the bi-spectral infrared detection (BIRD) experimental small satellite mission (2001–2004). *Remote Sensing of Environment, 100*, 29–51.